ADA035093

DNA 4015F

EXPERIMENTAL INVESTIGATION OF THE INTERACTION BETWEEN STRONG SHOCK WAVES AND WATER DROPLETS

Acurex Corporation/Aerotherm Division
485 Clyde Avenue
Mountain View, California 94042

July 1975

Final Report for Period September 1973—August 1975

CONTRACT No. DNA 001-74-C-0051

APPROVED FOR PUBLIC RELEASE;
DISTRIBUTION UNLIMITED.

D D C

RECEIVED

FEB 1 1977

D

Prepared for
Director
DEFENSE NUCLEAR AGENCY
Washington, D. C. 20305

Destroy this report when it is no longer
needed. Do not return to sender.

REPORT DOCUMENTATION PAGE		READ INSTRUCTIONS BEFORE COMPLETING FORM
1. REPORT NUMBER DNA 4015F	2. GOVT ACCESSION NO.	3. RECIPIENT'S CATALOG NUMBER
4. TITLE (and Subtitle) EXPERIMENTAL INVESTIGATION OF THE INTERACTION BETWEEN STRONG SHOCK WAVES AND WATER DROPLETS		5. TYPE OF REPORT & PERIOD COVERED Final Report for Period September 1973—August 1975
		6. PERFORMING ORG. REPORT NUMBER 75-156
7. AUTHOR(s) N. A. Jaffe		8. CONTRACT OR GRANT NUMBER(s) DNA 001-74-C-0051
9. PERFORMING ORGANIZATION NAME AND ADDRESS Acurex Corporation/Aerotherm Division 485 Clyde Avenue Mountain View, California 94042		10. PROGRAM ELEMENT, PROJECT, TASK AREA & WORK UNIT NUMBERS NWED Subtask N99QAXAA129-30
11. CONTROLLING OFFICE NAME AND ADDRESS Director Defense Nuclear Agency Washington, D.C. 20305		12. REPORT DATE July 1975
		13. NUMBER OF PAGES 54
14. MONITORING AGENCY NAME & ADDRESS(if different from Controlling Office) Aerotherm-75-156		15. SECURITY CLASS. (of this report) UNCLASSIFIED
		15a. DECLASSIFICATION/DOWNGRADING SCHEDULE

16. DISTRIBUTION STATEMENT (of this Report)

Approved for public release; distribution unlimited.

17. DISTRIBUTION STATEMENT (of the abstract entered in Block 20, if different from Report)

18. SUPPLEMENTARY NOTES

This work sponsored by the Defense Nuclear Agency under Subtask N99QAXAA129-30.

19. KEY WORDS (Continue on reverse side if necessary and identify by block number)
Hydrometeors
Erosion
Shock Tube
Droplet Generator

20. ABSTRACT (Continue on reverse side if necessary and identify by block number)

The results of an experimental study on water droplet shock wave interactions are presented. The experimental facility employed on this investigation was the NASA Ames Research Center Electric Arc Shock Tube. Tests were conducted at free stream pressures ranging from 0.13 atm to 0.50 atm and shock velocities varying from 8.4 to 15.5 kfps on spherical droplets having diameters ranging from 53 μm to 180 μm. Spark shadowgraph pictures over time duration, after passage of the shock, of 4 μsec were obtained with a multiframing image

DD FORM 1473 EDITION OF 1 NOV 65 IS OBSOLETE

Cont

20. ABSTRACT (Continued)

converter camera. The results demonstrate the effects of shock waves on droplet break-up and drag. Correlations were obtained employing dimensionless times and displacements.

PREFACE

This document is the final report of an experimental study on water droplet/ shock interactions. The technical information reported herein has been developed by the Aerotherm Division of Acurex Corporation, located in Mt. View, California, in accordance with requirements specified by Contract DNA001-74-C-0051.

The work has been sponsored by the Defense Nuclear Agency, Washington, D.C. The NASA Ames Research Center Electric Arc Shock Tube was employed to obtain data. The Project Officer for this program has been Mr. Mort Rubinstein.

The author is indebted to Mr. H. Dehne and Mr. C. Wolf of Aerotherm and R. Dannenberg of NASA Ames for their supporting efforts.

1

TABLE OF CONTENTS

LIST OF ILLUSTRATIONS

LIST OF TABLES

4

SECTION 1

INTRODUCTION

Reentry vehicles may, depending on weather conditions, encounter water droplets and/or ice crystals at altitudes below 50,000 ft. The concentration of condensed phase water (hydrometeors) is typically on the order of hundredths to tenths of a gram per cubic meter for ice crystals in cloud formations and can be on the order of several grams per cubic meter for water droplets in rain fields. Due to high velocities a reentry vehicle can experience severe erosion damage arising from encounters with hydrometeors. In order to accurately predict erosion damage experienced by specific materials it is necessary to know hydrometeor impact mass and velocity. The values of the aforementioned quantities will be affected by phenomenon associated with interaction between the shocked gas layer surrounding the vehicle and the hydrometeors traversing this layer; these effects decrease with increasing hydrometeor size and decreasing shock strength. Consequently, in order to accurately assess erosion damage caused by variable size hydrometeors and variable vehicle geometries and flight conditions, it is necessary to understand and be able to quantify hydrometeor/shock interaction phenomenon. Thus an experimental program, utilizing a shock tube facility was initiated, directed at determining the effects of shocked gases on hydrometeors. To date this program has been successful in obtaining data relative to water droplet/ shock interactions and there is an on-going effort directed at establishing a data base relative to ice crystal/shock interactions. The present report documents the results and data correlations obtained from the water droplet tests.

There have been a number of previous investigations analytical and experimental in nature on particle gas interactions that, because of their relevance, should be cited. Early studies have been concerned with drag, heat transfer, mass transfer, and break-up of particles in moderate to high energy gaseous flow fields. Analyses of particle heating and drag for rocket nozzle environments are presented in References 1 through 3. References 4 and 5 contain treatments of mass transfer effects arising from chemical reactions for combustion chamber as well as nozzle environments. In the aforementioned references drag effects are modelled through the application of drag coefficient-Reynolds number correlations and heat transfer is modelled through the application of Nusselt No. correlations with Reynolds No. and Prandtl No.

More recently a number of analytic and experimental investigations have been conducted on droplet and ice crystal phenomenon behind shock waves (see References 6 through 17). References 6 through 8 treat weak shock wave effects; references 9 through 17 are specifically concerned with droplet and ice crystal shock interactions for reentry flight conditions. The earlier references (9 through 12) present experimental results, data correlations, and a limited amount of analysis. While the work described in References 13 through 17 is purely of an analytic nature.

The results documented in Reference 9 were for shock Mach numbers of 3, 6, 9, and 11 at pressures of 1 atm, 0.46 atm, and 0.184 atm, the lower pressures corresponding to higher Mach numbers. Water drop diameters were varied from 500μ to 2500μ, a range that is representative of naturally occurring rain drops. Droplet break up times and droplet displacement histories were obtained by piecing together information from single frame photographic data. In addition X-ray photography was employed to obtain mass histories. It was found that the displacement data could be correlated in terms of the parameters X and T where

$$X = x/d_0$$

$$T = (t\, U_2/d_0)\sqrt{\rho_2/\rho_L}$$

x = droplet displacement from unshocked location

U_2 = gas velocity behind shock

d_0 = unshocked droplet diameter

ρ_2 = gas density behind shock

ρ_L = droplet density

and the correlating function is given by

$$X = 0.8T^2$$

In addition it was found that at a sufficient time interval after passage of the shock the droplets broke up catastrophically, and a dimensionless break up time, T_b, could be obtained from the following Weber number correlation

$$T_b = 45/We^{1/4}$$

where

$$We = \frac{\rho_2 U^2 d_0}{\sigma}$$

σ = surface tension evaluated at conditions upstream of shock

Prior to times corresponding to T_b, mass loss was observed due to stripping. Application of the results of Reference 10 is restricted due to the limited range of test conditions. In that study only a single sized droplet was tested (approximately 500μ),

for the Mach No. range 3-4.3; upstream pressures ranged from 1 to 2 atm. At a Mach No. of 9 the free stream pressure was 0.014 atm; the altitude corresponding to this pressure is well above that for which atmospheric water droplets will exist. The results for drop displacement, Reference 10 with the exception of the high Mach No. low pressure case, are in reasonable agreement with those in Reference 9. For the high Mach No. case the droplet acceleration rates were higher; however, as was mentioned the test conditions for this case are not representative of reentry flight conditions.

A method for predicting water droplet trajectories through reentry vehicle shock layers including mass loss effects due to evaporation is presented in Reference 11; particle breakup phenomena is also discussed in this reference. The analysis utilizing numerous simplifying assumptions, starting with the equations of motion, develops closed form solutions for droplet coordinates (x,y) as a function of time as the droplet traverses the shocked gas layer. As a result of the simplifying assumption the equations of motion are uncoupled from the mass loss equation which is solved numerically. In References 13 and 14 an improved model for heat transfer is used to solve for the mass (size) variation with time and the equations of motion are coupled to the mass loss rate equation. It is pointed out that the solutions in Reference 12 are more general than those in References 13 and 14 from the standpoint that the former treats regions of stagnation and conical flow whereas, strictly speaking, the results in References 13 and 14 are valid only along the stagnation streamline.

An extension of the data base and analysis reported in Reference 9 is given in Reference 11; essentially Reference 11 presents results and data correlations covering smaller size droplets than the lower limit for tests reported in Reference 9. The principle correlating parameter in the aforementioned References is Weber No. and Reference 11 contains correlations, including results of other investigations, of droplet displacement and break up data over a five order of magnitude range of Weber No. The large scatter about the suggested correlations indicates that possibly other parameters, in addition to Weber No., are of importance.

Reference 15 represents the first attempt to model hydrometeor/shock interaction phenomena by solving the governing flow equations on a local level relative to the droplet. A two layer boundary-layer model is employed to describe heat and mass transfer events at the surface. The results indicate that heat and mass transfer effects are less than those predicted previously by applying global Nusselt No. correlations (i.e., References 13 and 14). It is felt that the results obtained using the more fundamental approach (i.e., Reference 15) showing smaller shock layer effects, are caused at least in part by neglect of the blocking effect on heat and mass transfer in Reference 13 and 14.

A sophisticated procedure for predicting particle trajectories including effects of heat transfer, mass transfer, and particle breakup is presented in Reference 16. The results in this reference are based on a programmed method of numerically solving the governing equations without relying on simplifying assumptions. Drag is treated by employing Reynolds No. correlations and heat transfer is treated in a global manner by applying correlations for Nusselt No. which include mass transfer effects. Subsequently this method has been applied to treating the effects of shock layers on hypervelocity impact induced erosion (Reference 17), coupled with thermal ablation.

The present investigation has been experimental and represents an extension of the work described in Reference 12. The time duration from droplet/shock encounter and test conditions for the present study were chosen to give results pertinent to the stagnation region of reentry vehicles. The bulk of the data was obtained utilizing an extremely high speed multi-framing camera in order to obtain a high resolution of events in the immediate region behind a shock front. The overall program objectives are to: (1) determine reentry vehicle shock layer effects on hydrometeor breakup and (2) determine reentry vehicle shock layer effects on hydrometeor impact velocity. The approach adopted to accomplish the aforementioned objectives consists of (1) utilization of a high energy (NASA AMES EAST Facility) shock tube to generate test conditions, (2) coupling droplet generator to shock tube test section, (3) utilization of high speed multiframing (Hadland Imacon) camera to obtain data — 8 to 16 total frames at framing rates up to 20×10^6 per second.

It is pointed out that there are two advantages of a multiple framing capability relative to that of a single framing capability, namely: (1) greater efficiency in data acquisition, and (2) improved accuracy. The first advantage stems from the fact that multiple data points, corresponding to different distances between shock front and hydrometeor can be obtained for each test condition, with a single frame camera only at a rate of one point per shot. The second advantage stems from the fact that error sources exist in a data set obtained with a single frame camera that are automatically eliminated with a multi-frame camera; examples are (1) uncertainty in initial droplet position — resulting in errors of measured droplet displacement, (2) uncertainty in initial droplet size — resulting in erroneous scaling utilized in dimensionless correlations, (3) uncertainty in shock location. That is, in order to deduce a sequence of events experienced by a single droplet from single frame data it is assumed that variation in test conditions, droplet size, and droplet location are negligible from test to test. Furthermore, it implies an extremely high degree of accuracy of instruments employed to locate shock.

The following sections describe the test equipment, test results, data correlations, and the application of the correlations to the prediction of shock layer effects on erosion attenuation.

SECTION 2

EXPERIMENTAL APPARATUS

The essential components of the experimental apparatus are the shock tube and driver, the water droplet generator, high speed camera, light source and accompanying optics. Mounted within the shock tube is a test section with windows and fixtures needed to accommodate the light source, optics, and droplet generator. The following sections describe the aforementioned components.

2.1 SHOCK TUBE, DRIVER, AND TEST SECTION

The NASA AMES Electric Arc Shock Tube (EAST) Facility was employed in this study to generate test conditions. A drawing of the facility and its peripheral elements is shown in Figure 2-1. The shock tube has a 4 inch internal diameter and an 8 inch outside diameter. The outer cross section of the test section is a square having side length seven and one-half inches. The inner cross section is circular and matches that of the shock tube. The overall length of the tube is forty feet. The downstream end discharges into a 296 ft^3 dump tank. The tube contains ports for ion probes, pressure gauges and photomultipliers. The positions of these ports are given in Figure 2-1. The dimension given for each station is the distance from that station to the driver exit plane. A membrane which ruptures during discharge is located at the driver exit plane.

The ion probes, designed and made by Ames Research Center, measure shock position as a function of time. The sensor is a twin electrode probe mounted in the wall of the tube with a small dc voltage impressed across the electrodes. A power supply, amplifier, and gate pulse generator complete the instrument. For additional details on this instrument see Reference 18. The pre-shot shock tube pressure is obtained from a Wallace and Tiernan gauge located at F_1. A Kistler gauge for obtaining pressure during a shot is located at L-3.

The energy producing the shock is produced by an electric discharge in the driver. The driver chamber is conical with the high voltage electrode located in the center of the small end of the cone; a ring shaped wall flush electrode is located at the larger, downstream end of the driver chamber. Energy for the driver is supplied
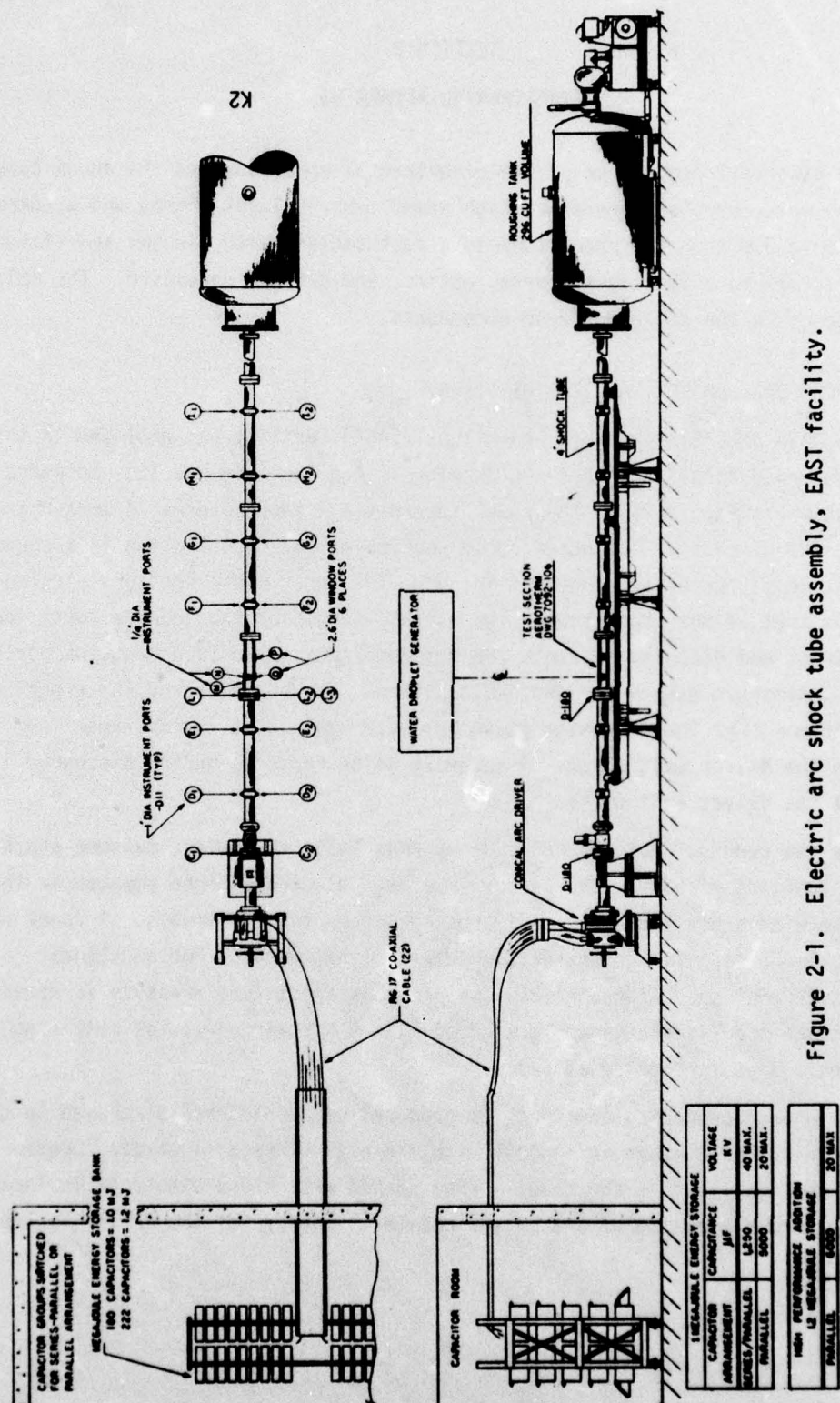
Figure 2-1. Electric arc shock tube assembly, EAST facility.

CAPACITOR ARRANGEMENT	CAPACITANCE μF	VOLTAGE KV
1 MEGAJOULE ENERGY STORAGE		
SERIES/PARALLEL	1,250	40 MAX.
PARALLEL	5000	20 MAX.
HIGH PERFORMANCE ADDITION 1.2 MEGAJOULE STORAGE		
PARALLEL	6000	20 MAX.

by a 1250-μ Farad capacitor bank rated at 10^6 joules when charged to 40 Kilovolts. Helium, hydrogen and argon driver gases have been employed; in the present tests hydrogen was used. It should be pointed out that the basic shock tube independent variables for a given test are capacitor charging voltage and shock tube pressure; the former quantity determines the capacitor storage energy. An oscilloscope trace of the current-voltage history, during discharge for a typical test is shown in Figure 2-2. Figure 2-3 shows the facility operating limits during the present program. The curve represents an upper limit on attainable velocity for a given pressure; the capacitor voltage drop for this curve is nominally 15 − 17.5 KV. Although the capacitor is designed to higher voltage drops; higher voltages do not produce higher gas velocities due to increased losses. Figure 2-3 also shows the facility operating conditions that are currently attainable using a modified driver. Further details on the NASA Ames EAST Facility are given in References 19 and 20.

2.2 DROPLET GENERATOR

Consistent with test objectives of the present program a system was developed capable of generating water droplets ranging in sizes down to 50 μm diameter spheres. Accurate positioning as well as size control was a requirement. Depth of field and field of view constraints necessitated that the droplet trajectories fall within a predetermined location not greater than 0.1 mm wide and 0.1 mm deep.

Two droplet generating techniques were considered. The first was originally developed by Abbott and Cannon (Reference 21) at the National Center for Atmospheric Research. The Abbott and Cannon generator utilizes a wire which is repeatedly inserted into and withdrawn from a water reservoir. During each withdrawal a cylindrical filament of water is removed from the surface. When the filamenter reaches a certain length it breaks off and contracts into a spherical drop. The size of the droplet is a function of the diameter of the wire, and angle between the wire and surface of the reservoir, and the depth of penetration of the wire into the reservoir. The droplet once formed is acted on by gravity. This method is extremely versatile and can produce droplets ranging in diameter from several hundred microns to submicrons. A disadvantage, however, is that due to slow settling velocity (0.2 ft/sec for 50 μm diameter droplets), stray air currents will cause large amounts of drift; this greatly reduces the probability of obtaining droplets at the desired location. For this reason a pulsed jet type of generator was used (see References 22 and 23). In these generators water in a pressured reservoir, with a feed line, exits a small diameter nozzle or orifice. Pressure pulses are obtained through an amplifier-oscillator system which feeds a signal to a piezoelectric crystal either in contact with the reservoir surface or the liquid itself. The pulses introduces an instability in the free jet exiting the reservoir which results in breakup and subsequent droplet
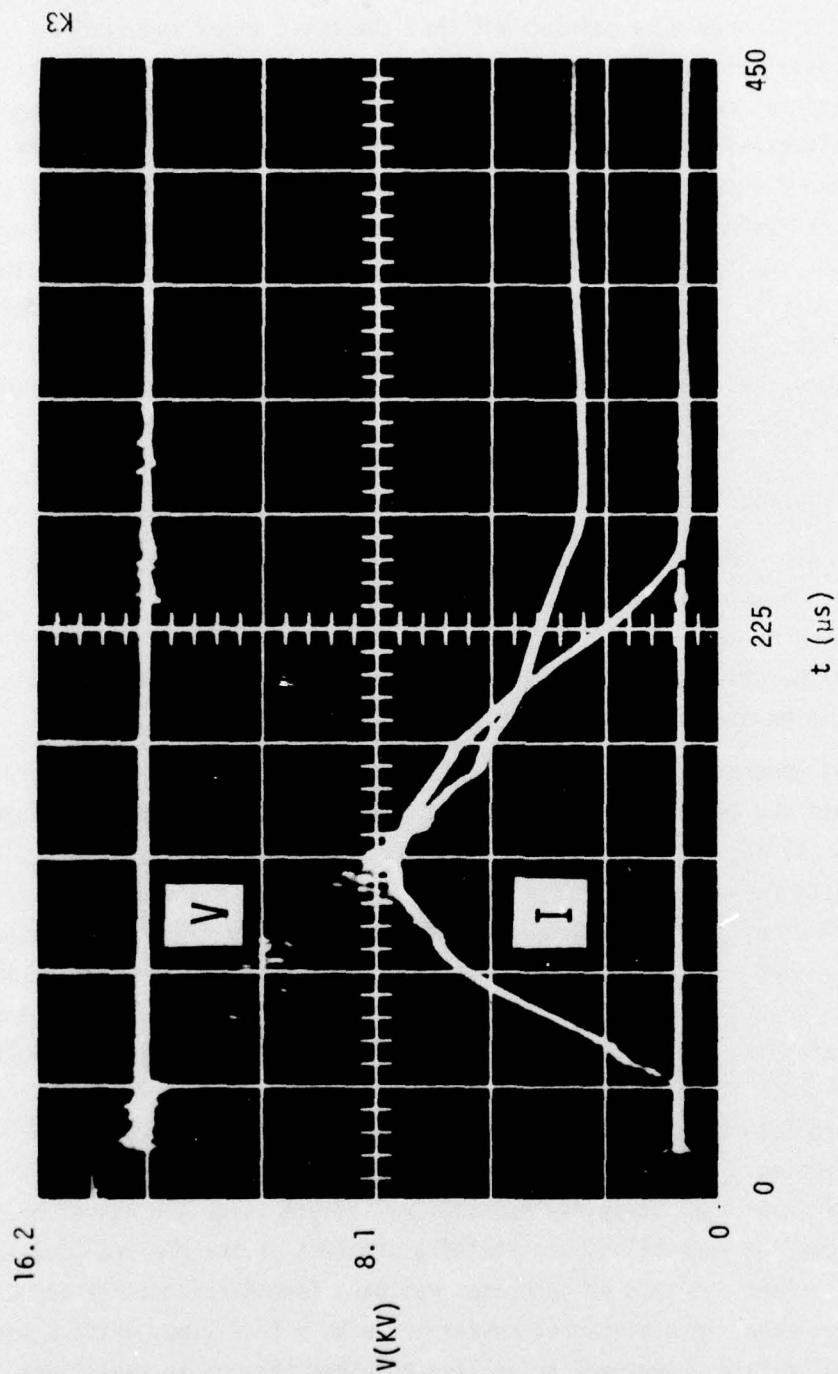
Figure 2-2. Driver characteristics, [E_d = 350 Kilojoules, P_∞ = 0.13 atm, V_∞ = 12.2 Kfps (measured at Station L)].
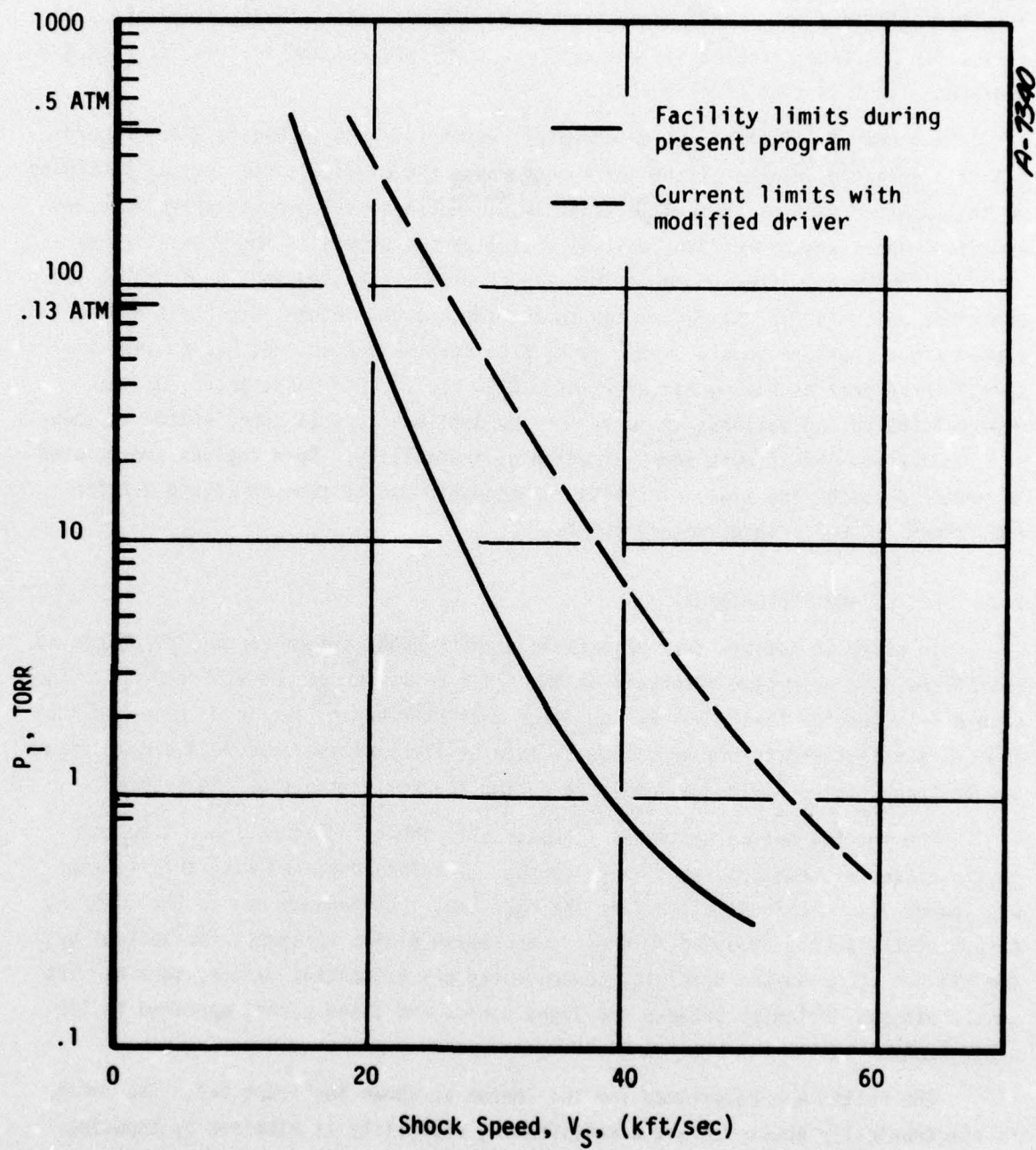
Figure 2-3. East facility operating characteristics.

formation. This type of generator can generate droplets at a greater rate ($10^3 - 10^4$ droplets/sec) than the Abbott generator and at greater velocities (approximately 50 ft/sec for 50 μmeter droplets). The size range of interest and desired accuracy was achieved with this type of generator.

A schematic of the droplet generator system is shown in Figure 2-4. Figure 2-5 is a detailed drawing of the nozzle assembly; the piezoelectric crystal is bonded to the upper surface of the nozzle assembly. A Heath signal generator and McIntosh amplifier operating off of line voltage activates the crystal. The insulation section and components attached to it (see Figure 2-4) are housed in a pressure sealed container which is directly connected to the shock tube. Other components of the system are a pressure supply, water tank, flow control valves, rotameters, and filters. Three nozzles having diameters of 0.0011 inch, 0.003 inch, and 0.008 inch were calibrated. A calibration curve for the smallest (0.0011 inch) nozzle is shown in Figure 2-6. This figure shows a region of instability. Such regions are related to nozzle diameter and flow rate; this relationship can be seen in Figure 2-7 for the largest (0.008 inch diameter) nozzle.

2.3 OPTICS AND PHOTOGRAPHY

In order to satisfy test objectives a photography system capable of obtaining multiframe data over time intervals on the order of 1 microsecond was required. The camera selected for this study was an image converter having the trade name Hadland Imacon, manufactured in England. Due to late delivery of the Imacon, a single framing Beckman Whitley camera was employed during the early stages of the program.

The initial optics system is schematically shown in Figure 2-8. A spectrophysics laser was employed as a light source. The data obtained with this system was low quality. This resulted from the fact that interference due to the coherent nature of the source produced fringes on the image plane; moreover, the optical system did not focus on the droplets, consequently any extraneous object, such as dirt on the windows or lenses between the light source and image plane, appeared in the photographs.

The system was redesigned for the Imacon as shown in Figure 2-9. The Imacon is electronically shuttered and a multiframing capability is attained by exposing sequentially different portions of a sensitized tube. Various tubes sensitive to light ranging from infrared to ultraviolet can be employed with the Imacon. For the present program an S-11 tube was used. Various plug in units can be used having different framing rates and exposure times. The following table lists the various options for recording eight 16mm x 18mm images or sixteen 16mm x 9 mm images.
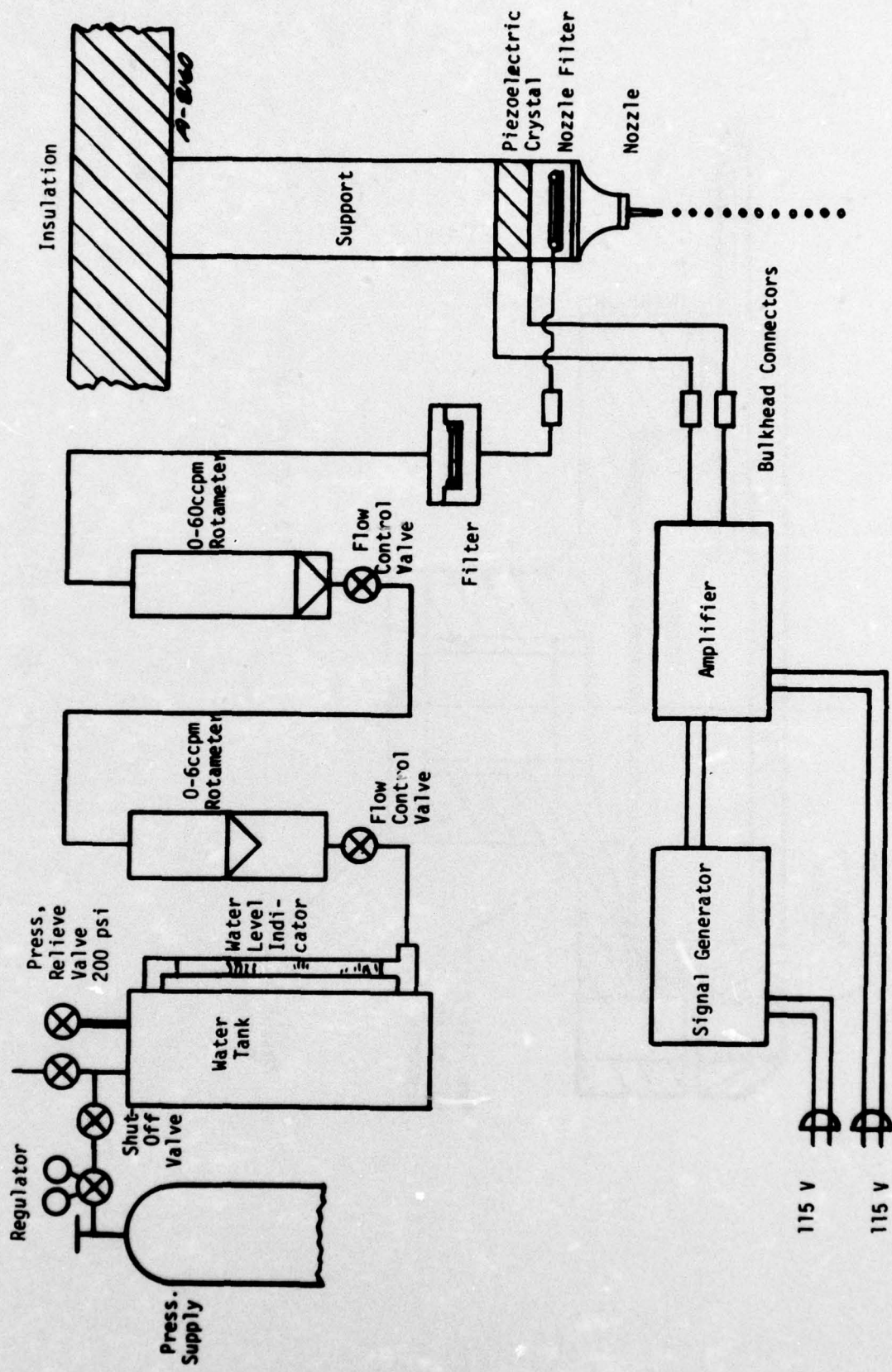
Figure 2-4. Droplet generator system schematic.
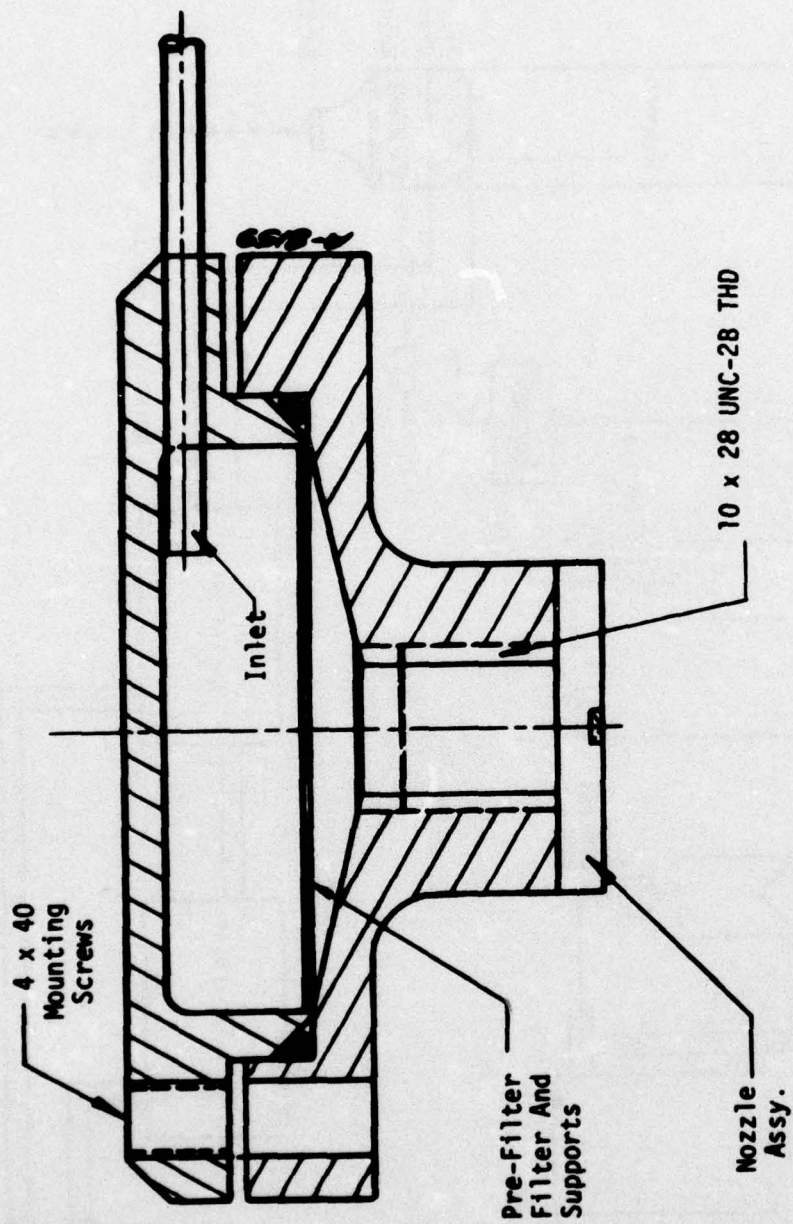
Figure 2-5. Nozzle assembly.
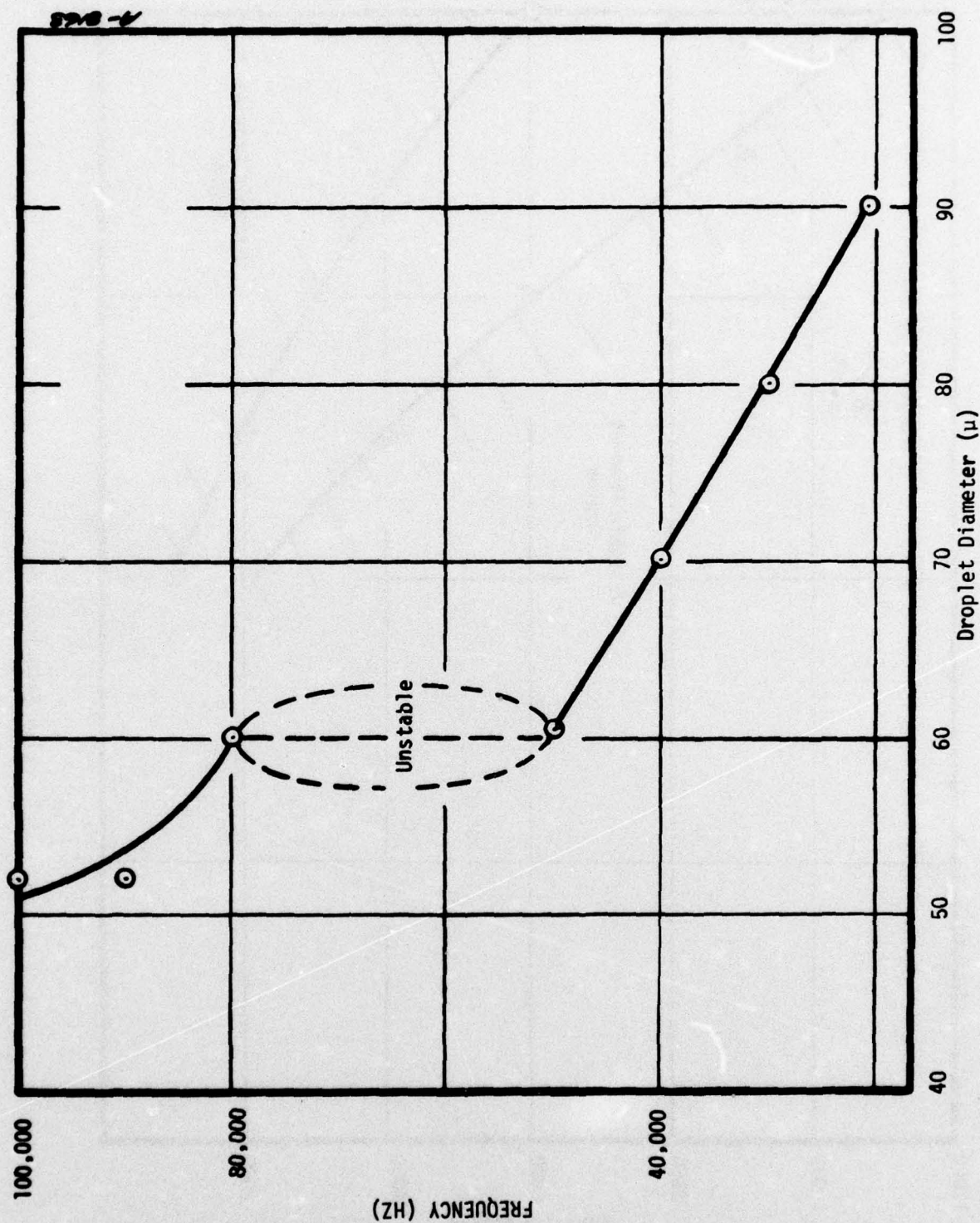
Figure 2-6. Droplet size - Frequency relationship.
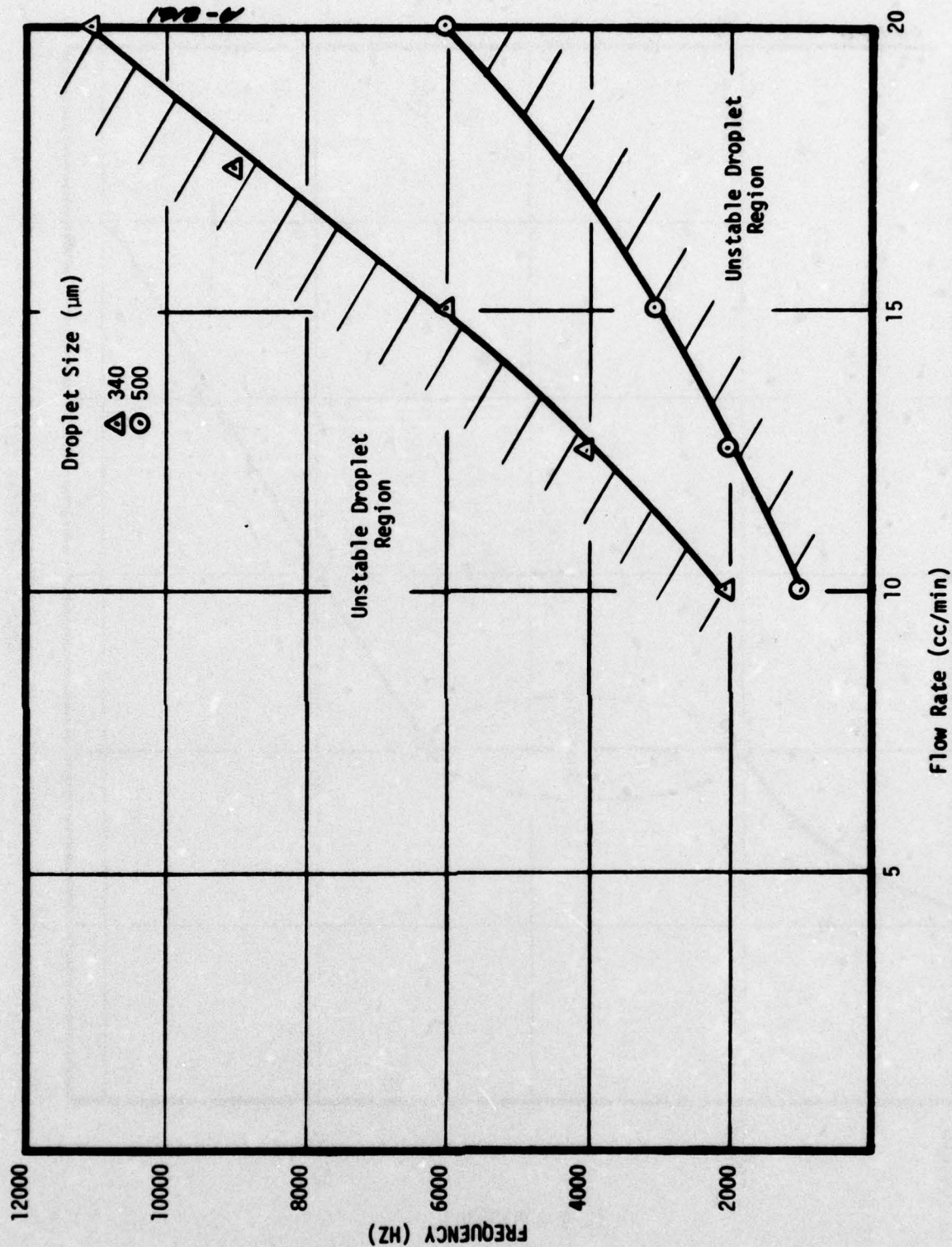
Figure 2-7. Droplet size, frequency, flow rate relation for 0.008 inch diameter nozzle.
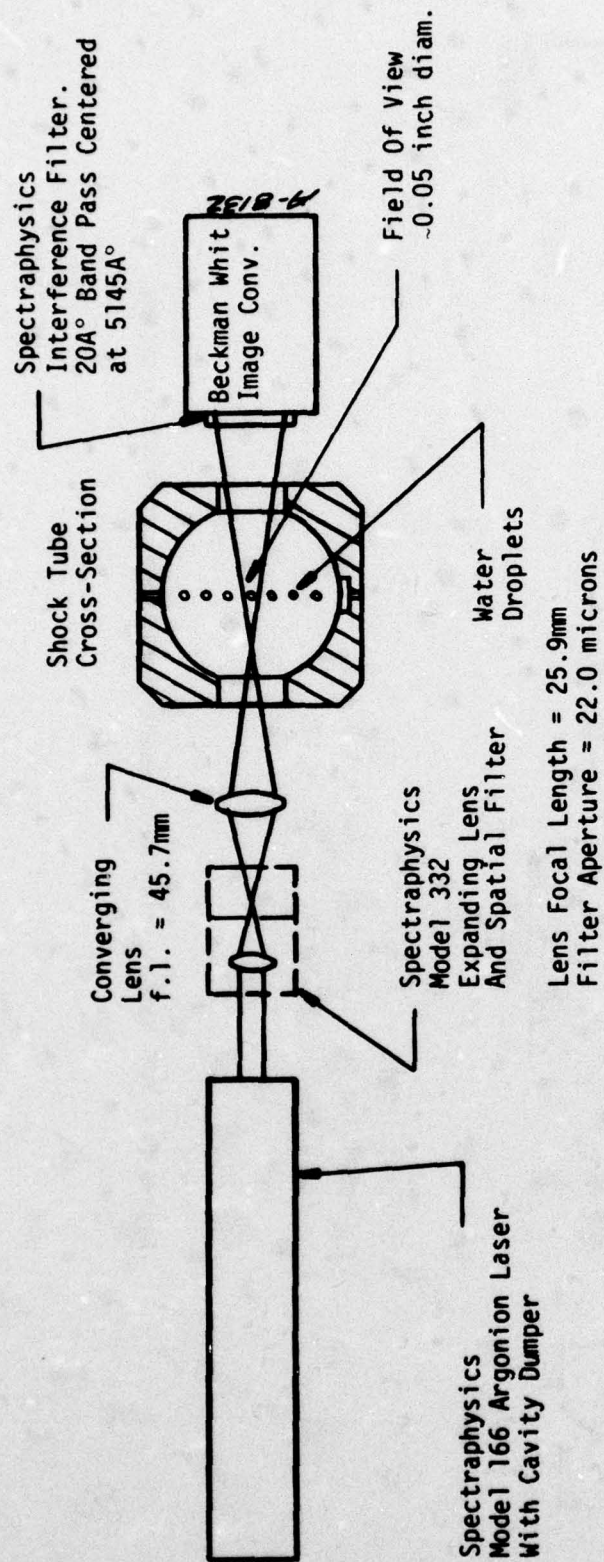
Figure 2-8. Schematic diagram of laser shadowgraph photography system.

L₁ = focal length = 21 mm
L₂ = focal length = 127 mm, f – no. = 1.9
L₃ = focal length = 1000 mm, f – no. = 12
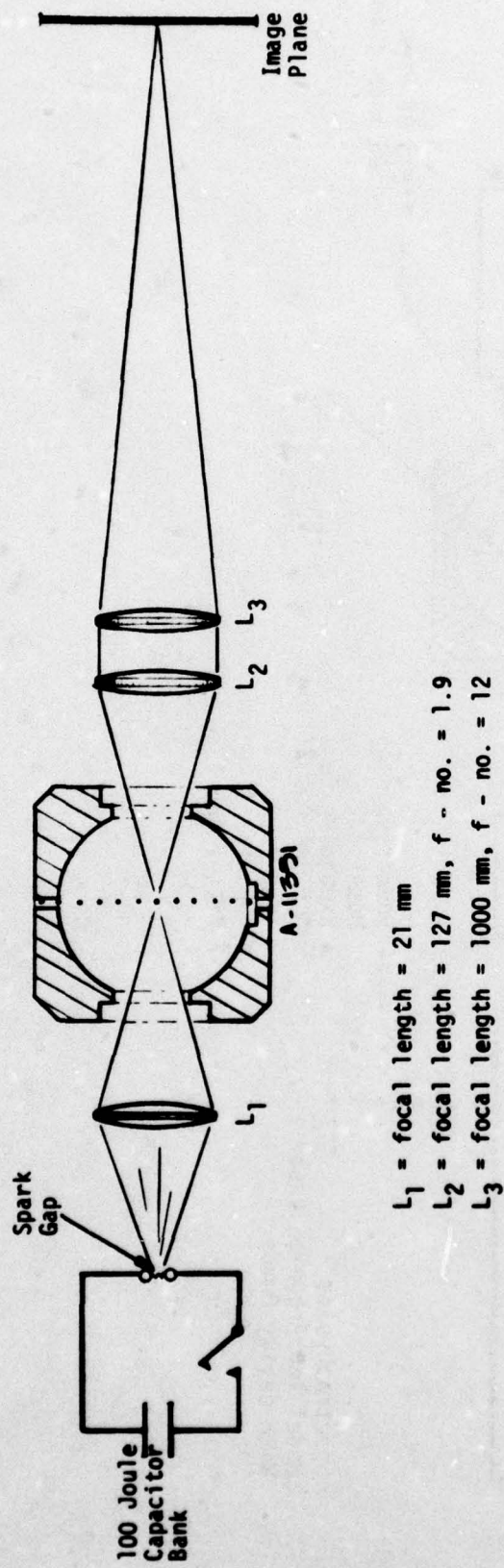
Figure 2-9.   Schematic diagram of spark shadowgraph photography system.

TABLE 2-1. TRIGGER MODE PLUG IN UNITS FOR HADLAND IMACON

Framing Rate (Sec^{-1})	Exposure Time (Sec) x 10^9
2×10^6	100
5×10^6	40
1×10^7	20
2×10^7	10

The first two units were employed on the present program giving total recording times of 4 μsec (x 10^6 frames per second) and 1.6 μsec (5 x 10^6 frames per second).

A photograph of the test section, droplet generator, and Imacon is shown in Figure 2-10. A water removal system was also installed to eliminate the formation of puddles and splashing. The removal system consisted of a filter mounted directly under the droplet stream flush with the wall of the shock tube connected by a drain line to a collection tank. The collection tank was connected to a vacuum pump and instrumented with a pressure gauge. In addition to eliminating splashing, the water removal system eliminated spurious results, such as were reported in Reference 10, arising from alteration of shock properties due to the presence of water vapor.
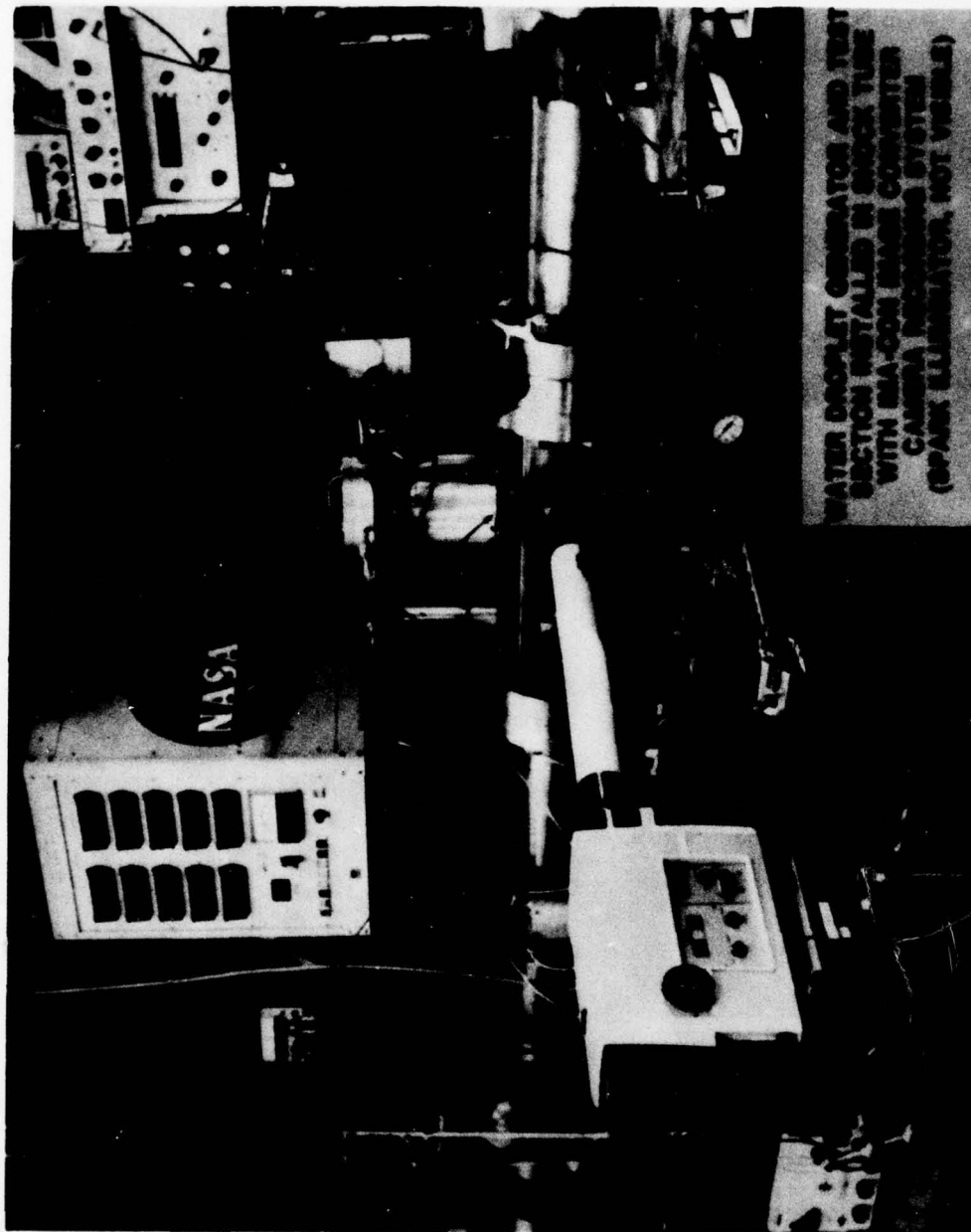
Figure 2-10. Test section, droplet generator, camera assembly.

2-14

SECTION 3

RESULTS AND ANALYSIS

Test results were obtained for droplet diameters ranging in size from 53μm to 180μm, velocities ranging from 8.2 to 15.5 Kfps, and pressure ranging from 0.13 to 0.50 atm. A summary of test conditions and data for successful runs is given in Appendix A. Droplet distortion and droplet displacement data were obtained directly from the spark shadowgraphs obtained with the Hadland Imacon.

The camera was triggered by the ion probe located at station N with a time delay based on shock velocity. This delay is set prior to the shot and is a function of the capacitor voltage and pre-shot shock tube pressure. The shock velocity is not exactly repeatable leading to errors in computed pre-shot camera trigger delay times. This caused in some cases early camera triggering resulting in frames showing an unshocked droplet and in some cases late camera triggering resulting in missing early time events. In some cases for which the delay was set at too large of a value the droplet was swept out of the field of view by the shock wave prior to the completion of camera recording. It is pointed out that difficulties arising from uncertainty in trigger delay times could be circumvented by increasing total recording time; however, this results in a reduction of the time resolution of events.

3.1 EXPERIMENTAL RESULTS

Results based on 86 frames and 14 runs are tabulated in Appendix A. Figure 3-1 is an example of shadowgraph data. From approximately 80 data points of the type shown in Figure 3-1 a sequence of droplet deformation can be constructed; this sequence is shown in Figure 3-2. Assigned to each deformation stage shown in Figure 3-2 is a shape index varying from 0 to 7; 0 corresponds to the unshocked droplet and shape index; 7 corresponds to droplet fragmentation or break-up. Initially a small amount of mass is stripped from the droplet and it remains undeformed (shape index 1). Subsequently the droplet begins to dilate in a direction normal to the direction of motion of the shock wave (shape index 2). Then a tail begins to form (shape index 3), the tail widens and elongates (shape index 4), and becomes irregular (shape index 5); this is followed by the formation of waves on the front surface of the droplet (shape index 6) and finally fragmentation or break-up of the droplet takes place (shape index 7).

DNA HYDROMETEOR SHOCK INTERACTION PROGRAM
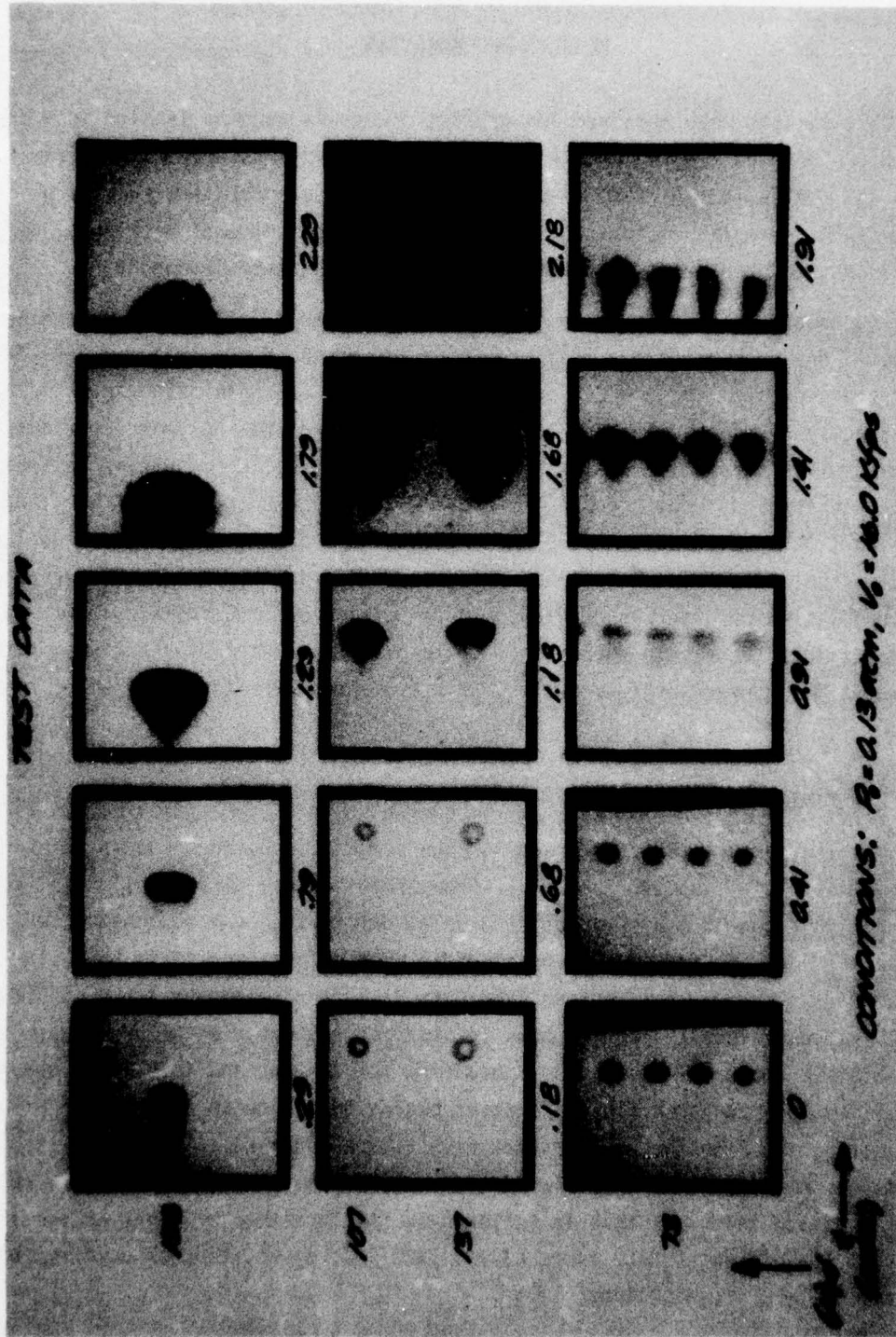
Figure 3-1. Selected frames from three tests.
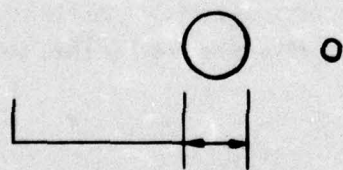
Figure 3-2. Droplet deformation.

In order to correlate the data, the following dimensionless parameters are introduced.

$$X = x/d_o$$
$$T = U_2 t/d_o \sqrt{\rho_\ell/\rho_2}$$

where x = droplet displacement

           d_o = undisturbed droplet diameter

           U_2 = gas velocity behind shock

           t = time measured from shock arrival at droplet

           ρ_ℓ = droplet density

           ρ_2 = gas density behind shock

Figure 3-3 shows the variation of the shape index defined by Figure 3-2 with dimensionless time T. Figure 3-4 shows dimensionless displacement data plotted as a function of dimensionless time. The scatter in shape index data is partially attributable to the fact that it is semi-quantitative in nature. Both the shape index data and displacement data indicate the shock layer effects to be smaller at a free stream pressure of 380 torr than 100 torr; that is, at 380 torr the shape index and displacement variation with dimensionless time is less than that at 100 torr. It is pointed out that the present data is in reasonably good agreement with the correlation of Engel's data but differs significantly from AVCO's correlation. The present data indicates, that early time droplet displacement takes place at a significantly lower rate than late time displacement. That is during early time, the measured rate of displacement is imperceptible, while at later times it varies almost quadratically with time. Moreover, the duration of this so-called early time behavior is longer at higher pressures (380 torr) than at lower pressures (100 torr). However, inconsistencies existed between photographic and ion probe data at high pressures; that is, the ion probe data indicated shock arrival times at the droplet approximately 4 μsec later than was indicated by photographic data. The times employed in Figure 3-3 and 3-4 for 380 torr data were obtained from photographic rather than ion probe information. Due to the inconsistency mentioned above the subsequent analysis weights the 100 and 190 torr data more heavily than the 380 torr data.

3.2 ANALYSIS

The results presented in the previous section of this report have been employed to predict shock layer attenuation of recession. In order to do this the effects of shock layers on impacting kinetic energy for a given droplet distribution must be determined. The analysis is carried out for conditions corresponding to those in the stagnation region of a reentry vehicle.
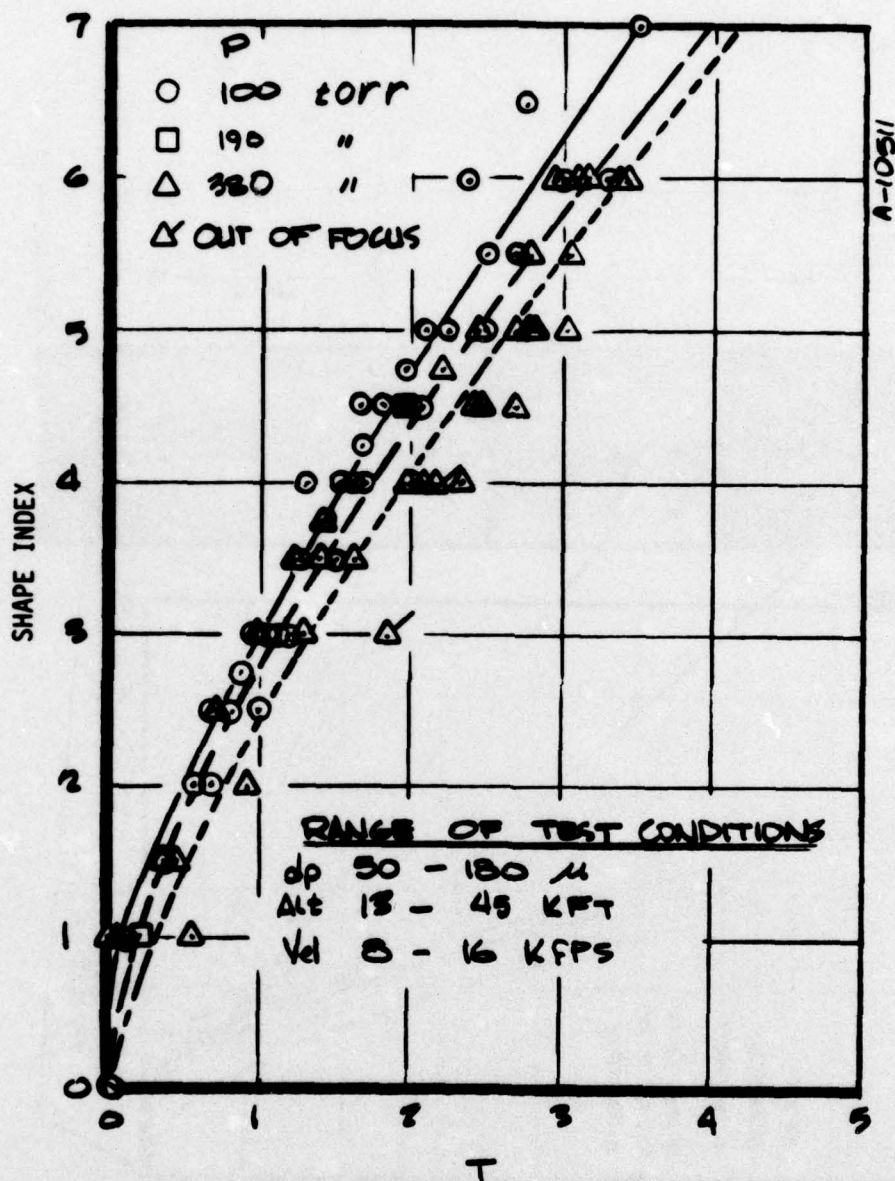
Figure 3-3. Shape index variation with dimensionless time parameter.

3-5
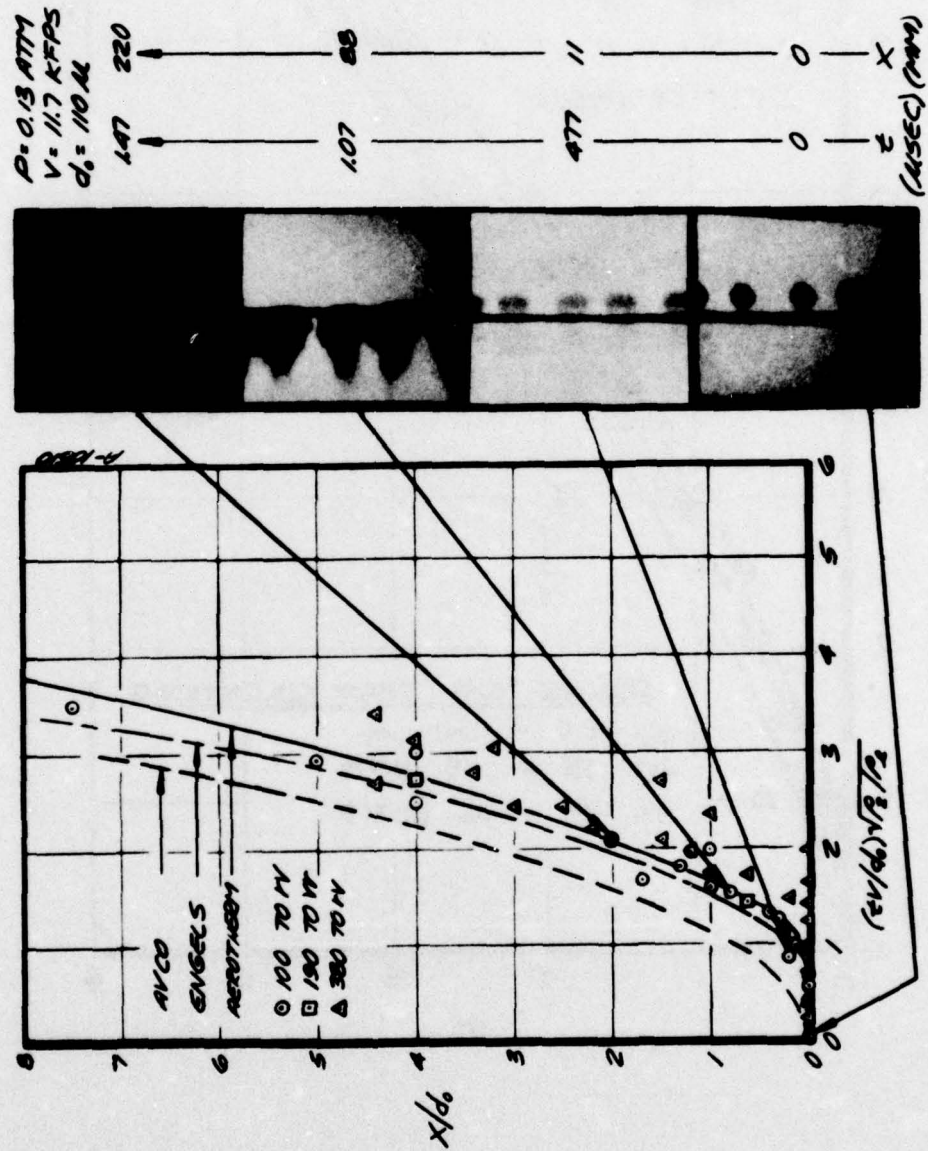
Figure 3-4. Droplet displacement data.

In body fixed coordinates the impact velocity, u_i, will be the relative velocity between the body u_∞ and the particle u_p at impact time t_i. That is

$$u_i = u_\infty - u_p(t_i) \qquad (3-1)$$

The particle velocity as a function of time can be obtained from the derivative of the displacement curve $x(t)$. Thus

$$u_p(t) = \dot{x}(t) \qquad (3-2)$$

The dimensionless impact velocity can be obtained from the derivative of the displacement curve shown in Figure 3-4 utilizing the following relation

$$V_i = 1 - (1 - \varepsilon)\sqrt{\rho_2/\rho_\ell} \, \dot{X}(T_i) \qquad (3-3)$$

where $V_i = u_i/u_\infty$

$\varepsilon = \rho_\infty/\rho_2$

ρ_ℓ = density of droplet

$U_2 = (1 - \varepsilon)u_\infty$

and the subscripts i, ∞, and 2 denote conditions at impact, in the free stream, and behind the shock wave, respectively. For reasons mentioned previously the lower pressure data is felt to be more accurate and this data has been weighted more heavily than the 380 torr data in the correlations. Consequently, the following correlation of displacement data has been adopted

$$\left. \begin{array}{ll} X = 0 & 0 \leq T \leq 0.75 \\[2mm] X = 0.5207 - 1.388\,T + 0.9256\,T^2 & 0.75 < T \end{array} \right\} \qquad (3-4)$$

The above two equations represent a reasonably good fit to the data while maintaining continuity of displacement, $X(T)$, and the dimensionless time derivation of displacement, $\dot{X}(T)$. As can be seen from Equation (3-3), the dimensionless impact time, T_i, is required in order to obtain V_i. The relative distance traveled, D, between the shock front and the body at time t is given by

$$D = u_\infty t - x(t) \qquad (3-5)$$

3-7

and the impact time, t_i, is obtained by replacing D with the shock stand-off distance, Δ_s giving

$$\Delta_s = u_\infty t_i - x(t_i) \qquad (3-6)$$

Consequently the dimensionless impact time is obtainable from

$$\bar{\Delta} = T_i/(1 - \epsilon)\sqrt{\rho_2/\rho_\ell} - X(T_i) \qquad (3-7)$$

where $\quad \bar{\Delta} = \Delta_s/d_o$

Δ_s = shock stand-off

d_o = undisturbed droplet diameter

and the shock stand-off distance in terms of nose radius R_N is given by

$$\Delta_s = 0.78 \, \epsilon \, R_N$$

Thus for

$$\bar{\Delta} < .75/\sqrt{\rho_2/\rho_\ell}(1 - \epsilon)$$

the dimensionless impact time T_i is given by

$$T_i = \sqrt{\rho_2/\rho_\ell}(1 - \epsilon)\bar{\Delta} \qquad (3-8)$$

and for

$$\bar{\Delta} > .75/\sqrt{\rho_2/\rho_\ell}(1 - \epsilon)$$

$$T_i = \frac{Z - \sqrt{Z^2 - 3.702(\bar{\Delta} + 0.5207)}}{1.8512} \qquad (3-9)$$

where

$$Z = \frac{1}{\sqrt{\rho_2/\rho_\ell}(1 - \epsilon)} + 1.388$$

3-8

The present data was obtained for conditions representative of a reentry vehicle stagnation region. For this region, in contrast to that on a vehicle frustum, mass loss is dominated by catastrophic breakup characterized by a breakup time, T_b, rather than stripping. Thus for computing the impact of shock layers on erosion it will be assumed that the impacting mass is given by

$$m_i = m_o \quad T_i < T_b \left. \right\}$$
$$m_i = 0 \quad T_i > T_b \left. \right\} \tag{3-10}$$

Implicit in this assumption is that the droplet fragments vanish on a time scale that is small compared to the time it takes for the original droplet to fragment. This is reasonable since the fragments are small compared to the orginal droplet and since they have been heated for a significant period of time. However, for a number of reasons this assumption is not critical. The result of this assumption is that the kinetic energy of impacting particles below a critical diameter is zero. As will be shown, the kinetic energy of particles in the region of breakup has already decreased significantly due to drag effects and for most flight conditions will become negligibly small for T_i 20 percent greater than T_b using the existing displacement correlation. Moreover, the predicted effects integrated over a droplet size distribution will be shown to not be a very sensitive function of breakup time due to the fact that most of the total mass entering the shock layer is distributed among particles having diameters greater than critical droplet diameters.

The data shown in Figure 3-3 has been employed to deduce breakup times. Three curves are shown plotted through the data, one curve is a least squares fit through the high pressure data, one through the 100 and 180 torr data and one through all of the data. Associating breakup with a shape index of 7 yields a breakup time range of 3.5 to 4.0. For reasons mentioned earlier, the high pressure data is suspect, consequently, it is felt that the low end of the above range represents a more realistic estimate of breakup time than the high end. Thus, a realistic estimate for breakup time is 3.5 whereas a conservative estimate (minimizing shock effects) is about 4.0. It will be shown that the net effect of the shock layer on erosion predictions does not vary significantly over a range of T_b from 2.75 to 4.0 for stagnation region conditions, thus, accurately pin-pointing the value of T_b is unnecessary.

Predictions based on the modeling described above are compared to those of AVCO; hence, it is appropriate to describe the methodology upon which the AVCO predictions are based. Impact velocities are obtained from the derivative of the following correlating function (Reference 9 and 12)

$$X = 0.8 \, T^2 \tag{3-11}$$

3-9

breakup is now given by (Reference 12).

$$T_b Q_m^{1/2} = 35/We^{1/4} \tag{3-12}$$

where $\quad We = \rho_2 U_2^2 d_0 / \sigma$

$\sigma = 75$ dynes/cm (surface tension at room temperature)

$Q_m^{1/2} = f (\rho, u) \approx 1$ for present test conditions

and breakup is determined by comparing T_i from Equation (3-7) to T_b from Equation (3-12).

In order to predict effects of shock layers on recession rate the following mass loss law is employed with both the AVCO and Aerotherm shock layer models

$$G = K_1 u_i^2 \tag{3-13}$$

The recession rate is then given by

$$\dot{s} = \dot{m}(K_1 u_i^2)/\rho_s \tag{3-14}$$

where $\quad K_1 =$ constant (material dependent)

$\dot{m} =$ mass flux of impinging particles

$\rho_s =$ density of surface material

$u_i =$ impact velocity

Therefore the ratio of recession rate including shock layer effects to that neglecting these effects $(\dot{s}_i/\dot{s}_\infty)$ is given by the following kinetic energy flux ratio

$$\frac{\dot{s}_i}{\dot{s}_\infty} = \frac{(\dot{m}u^2)_i}{(\dot{m}u^2)_\infty} = \dot{M}_i V_i^2 \tag{3-15}$$

The above equations can now be used to obtain the (s_i/s_∞) ratio as a function of altitude, velocity, nose radius, and particle diameter. In practice the droplets are distributed over a diameter range and in order to obtain the net effects of shock layers in flight, the above equation must be integrated over some suitable distribution function. As was mentioned, it will be assumed that all particles with diameters below the critical value d_c do not contribute to the erosion damage where d_c is the diameter of particles having impact time T_i equal to T_b. The following mass distribution function (Reference 24) is used for computational purposes

$$\mu(d_o) = \frac{1}{6\ D_m} \left(\frac{D}{D_m}\right)^3 e^{-D/D_m} \qquad (3\text{-}16)$$

where the mass mean diameter is $4D_m$.

The quantity (μdd_o) is the mass fraction of drops in the diameter range between d_o and $d_o + dd_o$. The actual recession rate ratio for a given distribution is now given by

$$\bar{\dot{s}} = \frac{\text{actual recession rate for given droplet distribution}}{\text{recession rate without shock wave}}$$

$$\bar{\dot{s}} = \int_0^\infty M_i V_i^2\ \mu(d_o)dd_o = \int_{d_c}^\infty V_i^2\ \mu_i(d_o)dd_o \qquad (3\text{-}17)$$

The preceding equations have been coded and predictions can be made for arbitrary combinations of altitude, velocity, R_N, D_m, and assumed dimensionless breakup time, T_b. A few examples will be presented for selected flight conditions and comparisons made with predictions using AVCO breakup times and accelerations.

According to the present model the shock layer attenuates recession by (a) reducing impact velocity, (b) shattering the droplet. Damage from droplets with impact time, T_i, greater than breakup time, T_b, will be reduced only due to deceleration. The dimensionless velocity, V_i, is a measure of the deceleration. It is of interest to compare dimensionless velocities predicted using the AVCO and Aerotherm displacement correlations. From equation (3-3) it can be seen that

$$V_i = 1 - F(\text{Alt., Vel.})\ \dot{X}(T_i) \qquad (3\text{-}18)$$

where

$$\dot{X}_{AVCO} = 1.6\ T$$

$$\dot{X}_{Aero} = 0, \qquad\qquad\qquad T < 0.75$$

$$X_{Aero} = 1.851\ T - 1.388, \qquad T > 0.75$$

Table 3-1 gives values for the quantity F, appearing in the above equation, at different values of altitude and velocity.

TABLE 3-1. VALUES OF COEFFICIENT F APPEARING IN EQUATION (3-18).

Alt. (Kft.)	Vel. (Kfps)	F
10	10	0.073
10	20	0.086
20	10	0.062
20	20	0.076

In order to compare dimensionless impact velocities, a nominal value of 0.074 is shown for F. Table 3-2 shows a comparison of impact velocities.

TABLE 3-2. COMPUTED IMPACT VELOCITIES FROM EQUATION (3-18)
FOR F = 0.074

T	V_i (AVCO)	V_i (Aero)
0	1	1
0.5	0.94	1
1.0	0.88	0.97
2.0	0.76	0.83
4.0	0.53	0.56

The differences between impact velocity are not large; however, their differences will lead to larger differences in recession rate due to the fact that recession rate varies as the kinetic energy of the impacting droplet.

The effect of the difference in impact velocity and break-up time on predicted recession rate as a function of droplet diameter is shown in Figure 3-5. The gradual recession rate drop off with decreasing droplet size is attributed to droplet velocity reduction, while the sharp drop off portion of the curve is attributed to droplet breakup. The differences between the present predictions and those of AVCO due to impact velocity are related only to differences in the displacement correlation discussed previously. The differences due to the breakup effect is related to differences in two factors: (a) displacement correlation, (b) breakup time. This arises
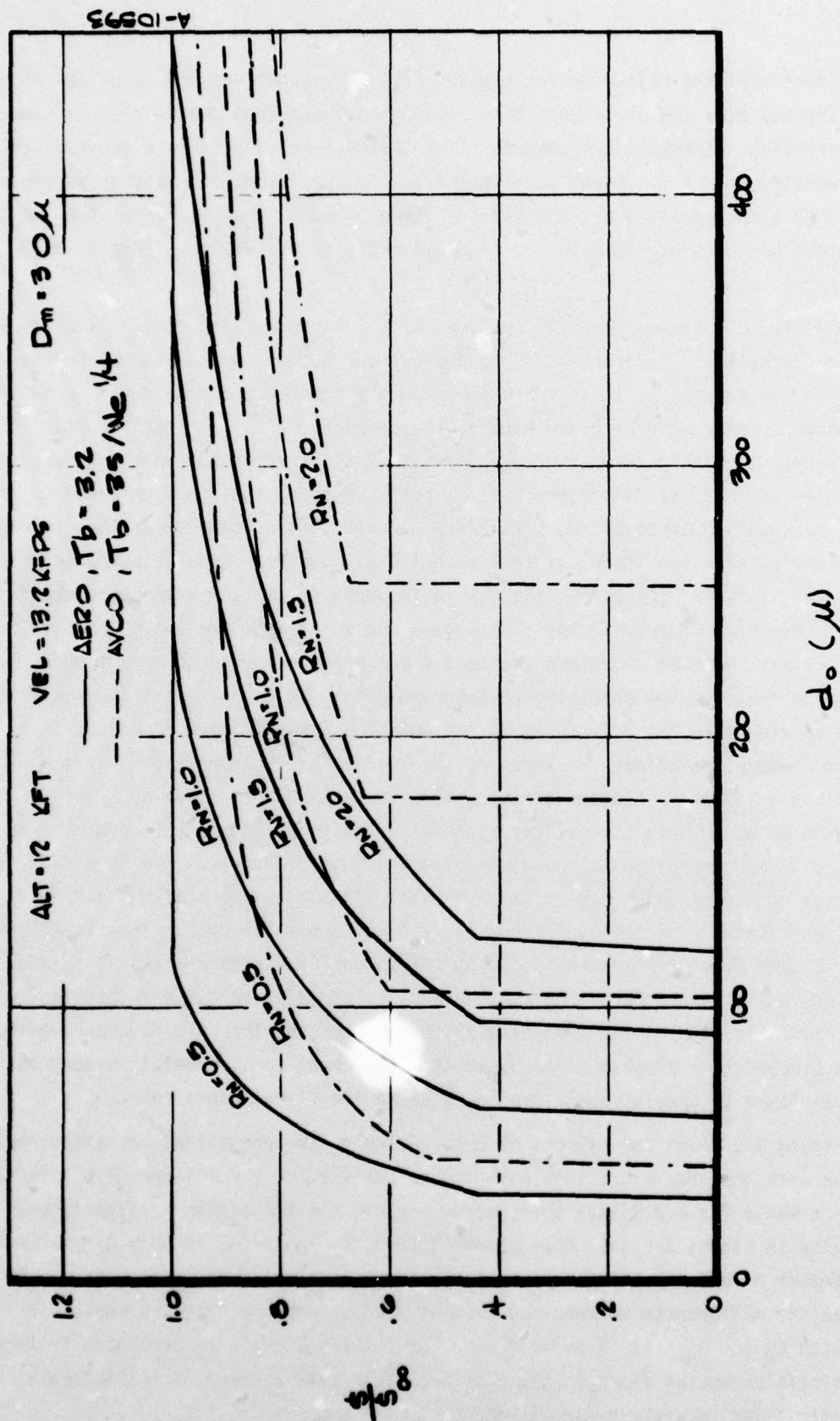
3-12

Figure 3-5. Effect of droplet size on recession rate.

from the fact that the criterion for breakup $(T_i, \geq T_b)$ involves both the impact time and the breakup time and the impact time, T_i, is computed from the droplet displacement correlation. Impact times computed from the AVCO correlation are greater than those predicted from the present correlation due to greater deceleration; moreover AVCO breakup times employed by AVCO are less than present values. Hence, the two factors mentioned above, contributing to differences due to breakup effects, both reinforce each other.

Differences between the AVCO and present values for breakup time are attributable to differences in interpretation of shadowgraph data. In the present investigation breakup in assumed at times corresponding to the onset of large waves (observed from shadowgraphs) on the windward side of the droplet. X-ray absorption data obtained by AVCO apparently indicates mass disappaerance at times prior to those corresponding to the onset of front surface waves. It is felt, however, that some uncertainty exits relative to interpretation of the x-ray data. It is single frame data, thus requiring a number of tests having identical test conditions, identical droplet size, and a variation of times for triggering the camera in order to capture a sequence event leading to breakup. Moreover, the shadowgraph and x-ray data are not taken simultaneously; hence, in order to relate the two, a process similar to that mentioned above must also be followed for obtaining shadowgraph data. It is felt that the possibility of error arising from the difficulty in implementing both of these processes in order to get one comparison between an x-ray picture and a shadowgraph exactly at the breakup time is significant. Another concern relative to the application of x-ray data is that it was obtained only for relatively large droplets ($>1000\mu m$). In order to apply this data to predictions of small droplet ($<100\mu m$) behavior, it is necessary to have a high degree of assurance relative to the validity of the scaling laws used. Lack of understanding of the basic physics related to breakup and a significant deviation of data from correlation involving the dimensionless parameters X, T, and We are indicative of the fact that further work is required relative to developing scaling laws. In view of the foregoing discussion and for the sake of conservativism, it is recommened that breakup times based on the present small droplet shadowgraph data be employed to predict small droplet breakup for flight conditions.

Figure 3-6 shows the effects of nose radius on the normalized recession rate. It can be seen that for a 0.5 inch nose radius vehicle the shock layer offers little protection while for a 2.0 inch nose radius vehicle the protection is significant. The results in Figure 3-6 have been cross plotted in Figure 3-7 to show droplet mass mean diameter effect on net recession; this effect is also significant. It can be seen that the differences between the present predictions and the AVCO curves increase with R_N and D_m. It it pointed out that the results can be presented in terms of the single parameter (R_N/D_m); the previous plots were presented to illustrate the effects separately of varying R_N and D_m.

3-14
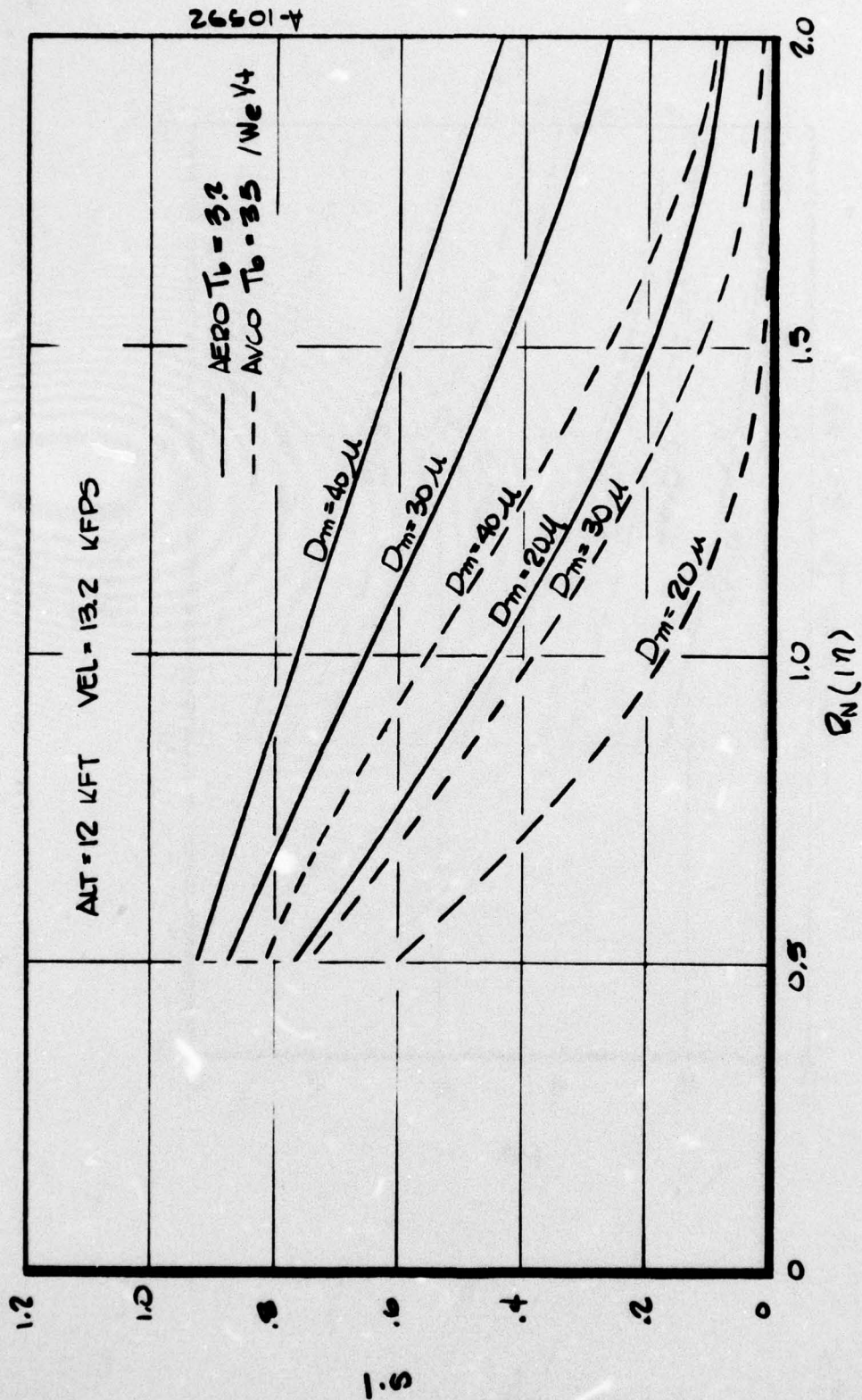
Figure 3-6. Effect of nose radius on $\bar{S}$.

3-15

ALT = 12 KFT   VEL = 13.2 KFPS

——— AEDO Tb = 8.2
– – – AVCO Tb = 35/We¹/⁴

$R_N = 0.5$
$R_N = 0.5$
$R_N = 1.0$
$R_N = 1.5$
$R_N = 1.0$
$R_N = 2.0$
$R_N = 1.5$
$R_N = 2.0$

A-10590

D_m (μ)

1-S

Figure 3-7. Effect of distribution reference diameter on $\bar{S}$.

Figure 3-8 illustrates shock layer effects for relatively low altitude clouds with large mean particle diameter. Although the trends are the same the effects are much less than for the higher altitude case. Also for this case the differences between the present and the AVCO predictions are much smaller than for the higher altitude case.

A limited sensitivity study was conducted in order to assess the effect of break-up time on predicted recession rate. The results are shown in Figure 3-9. The present data indicates dimensionless break-up times to be within the range of $3 - 4$. The sensitivity of S to T_b is strongly dependent on R_N. For nose radii less than 1 inch the variation of S over a range of T_b from 3 to 4 is less than 6 percent and for a range of T_b from 2 to 3 less than 19 percent. For a nose radius of 2 inch the variation of S with T_b is 15 percent over the range of T_b from 3 to 4. These results indicate that for the present set of flight conditions, the predicted recession rate is only moderately sensitive to break-up time. Also shown in this figure are AVCO values of S for break-up times given by Equation (3-12). Figure 3-9 illustrates that AVCO break-up times are significantly lower than the present recommended values of $(3 - 4)$. However, it can also be seen that for nose radii of less than 1.0 inch the differences in break-up time do not account for differences in S; indeed for $R_N = 0.5$ inch S does not vary with assumed T_b at all. For large R_N the predicted values do become sensitive to T_b for $T_b < 3.0$. From these results it is apparent that for nose radii less than 1.0 inch differences between the present results and those of AVCO are attributable mainly to differences in acceleration laws; for larger nose radii the differences are attributable to both differences in acceleration laws and differences in break-up time. It is of interest to compare the relative effects of droplet diameter on particle impact velocity, impact time, and deformation. These quantities are shown in Figure 3-10 and it can be seen that deformation is significant over a much larger range of d_o than break-up or acceleration. For example particles having diameters greater than 60μ will not break-up and acceleration is negligible for particles greater than 120μ, however, dilation is significant (i.e., 40 percent) for particles as large as 300μ. This observation is also made in Reference 25, based in part on Holloman sled data.
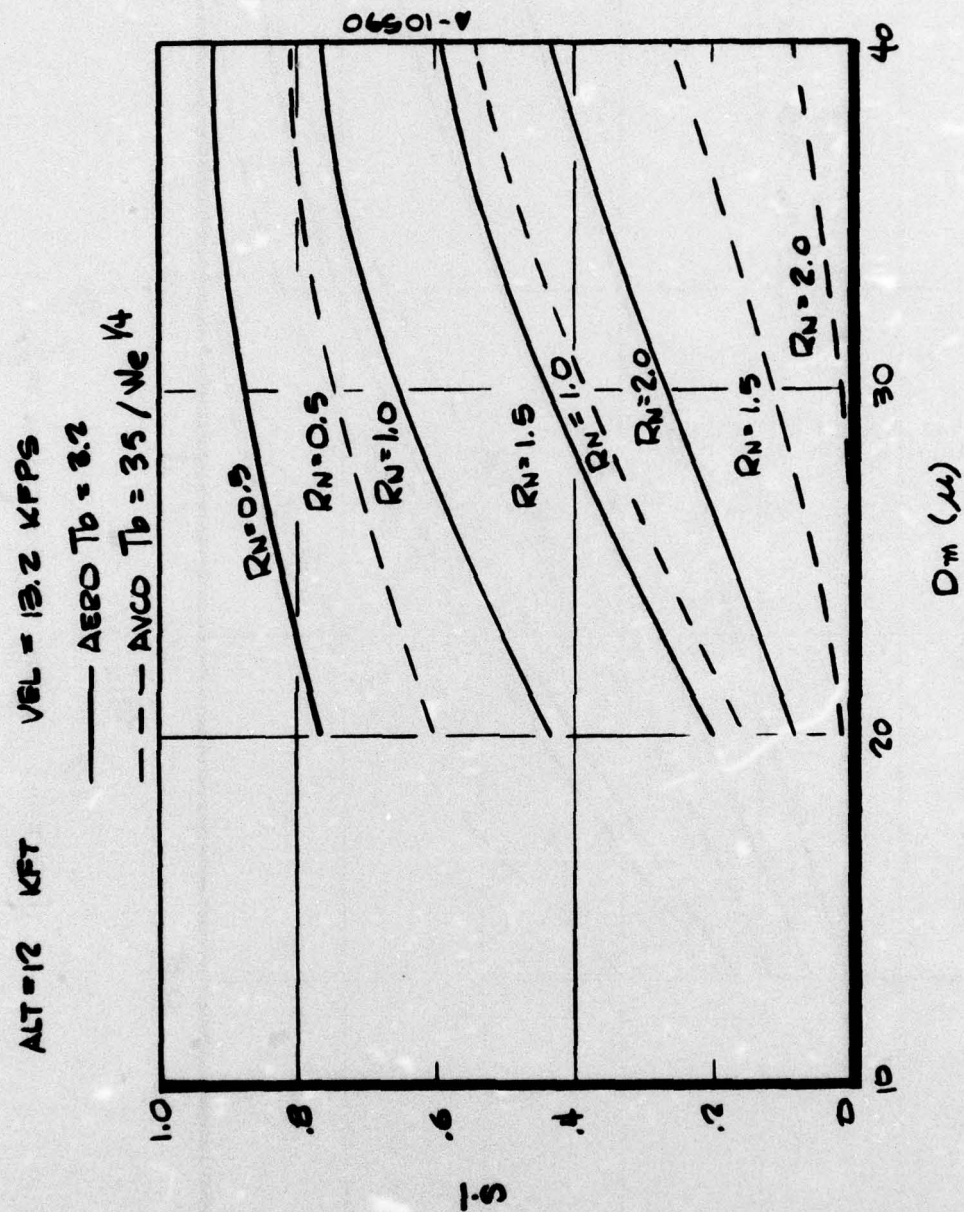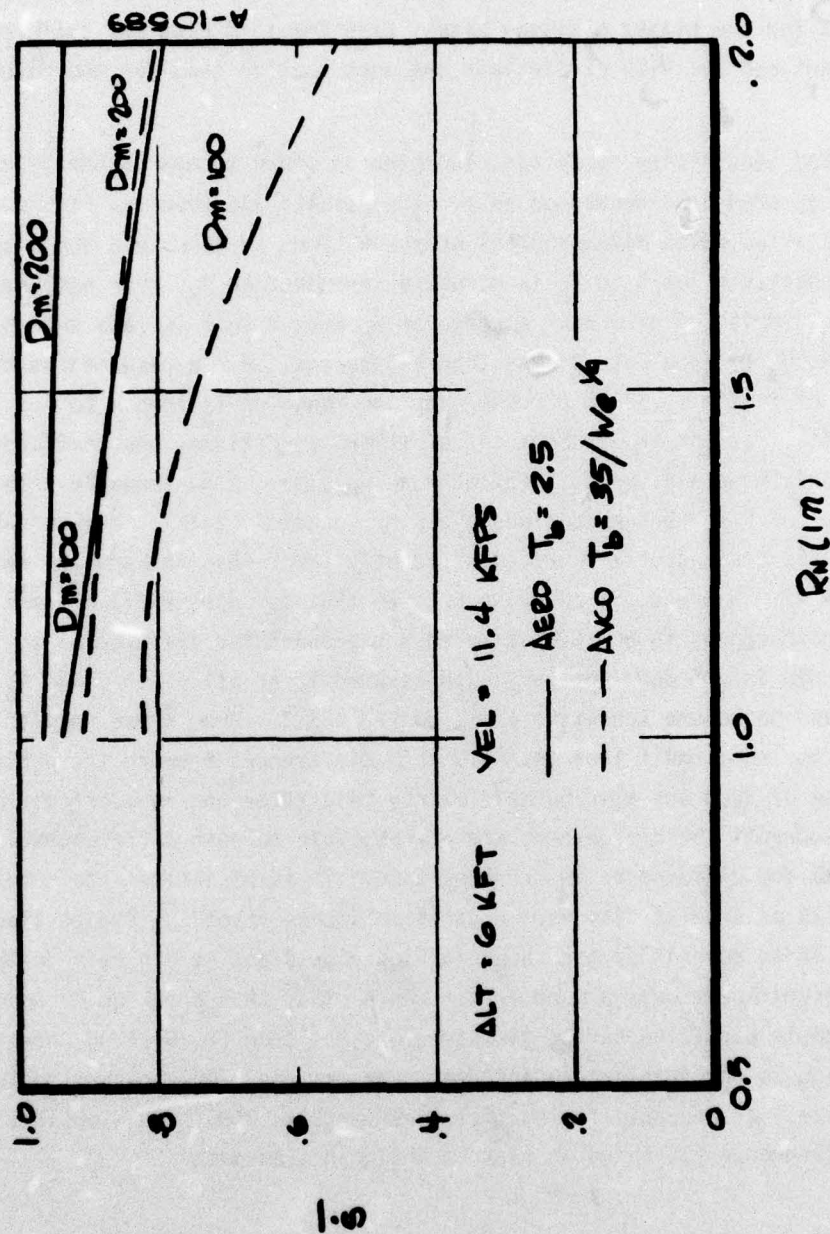
Figure 3-8. Effects of nose radius on $\bar{S}$.
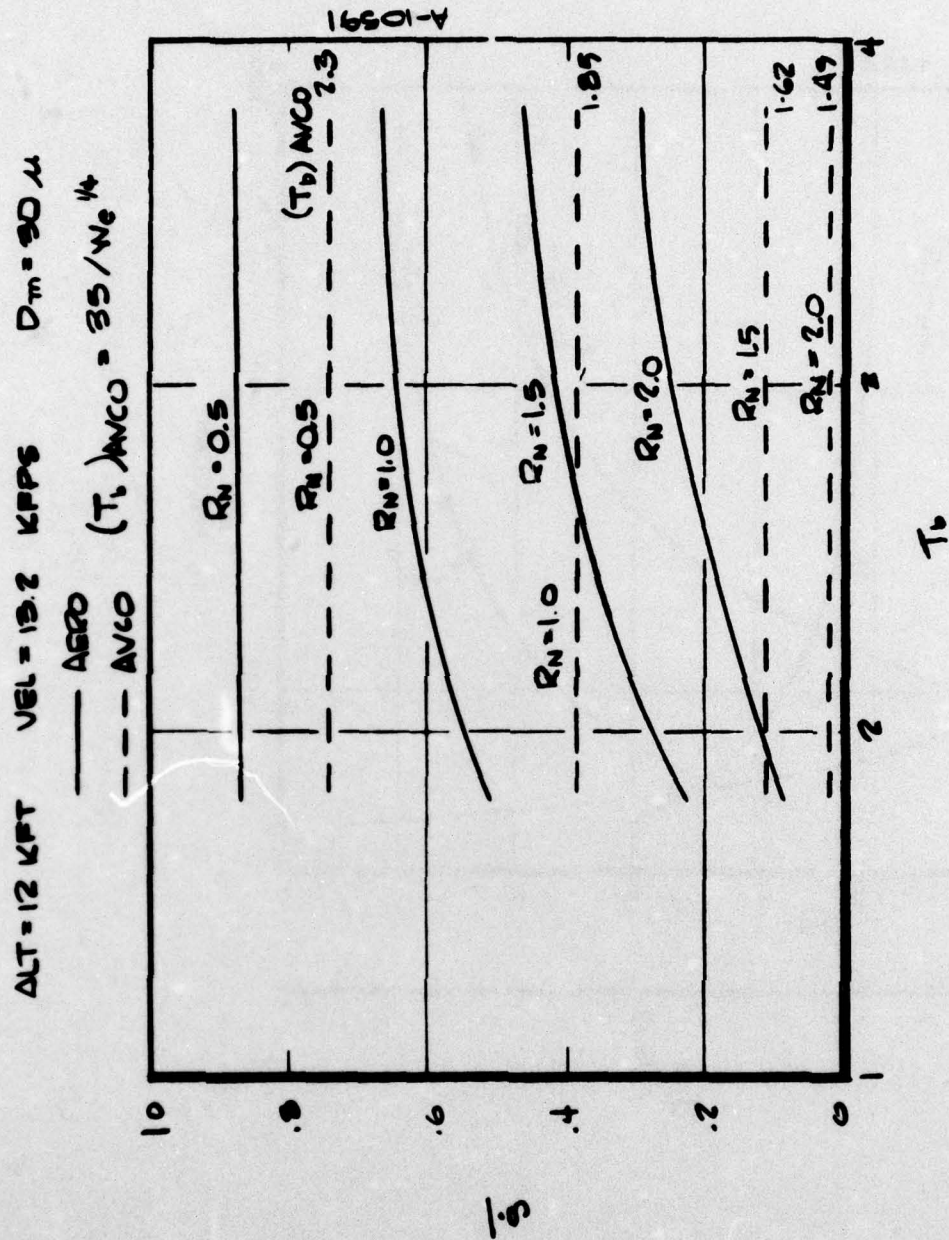
Figure 3-9. Effect of break-up time on $\bar{S}$.
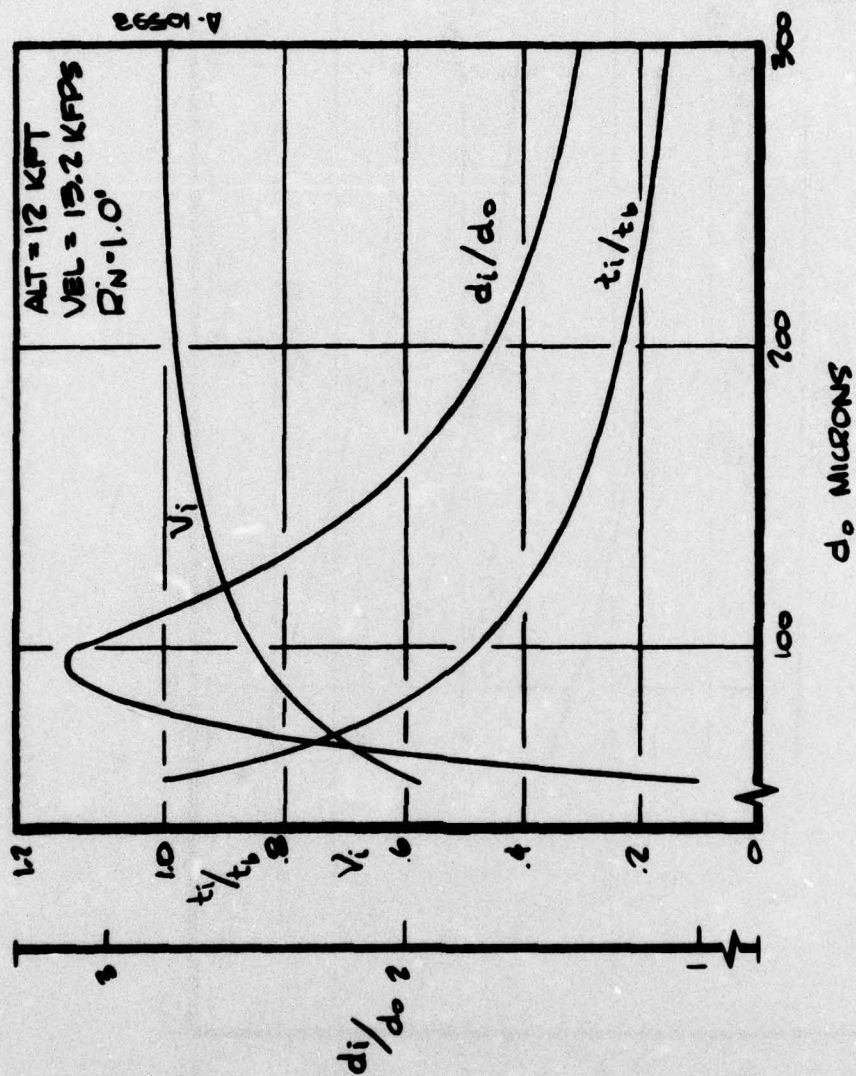
Figure 3-10. Droplet impact velocity, diameter, and time.

SECTION 4

CONCLUDING REMARKS

The effects of shock layers on droplet breakup time and acceleration have been measured. The data has been reduced and has been incorporated within a mathematical model of the effects of shock layers on stagnation point recession caused by hypervelocity flight through clouds of water droplets.

Predictions of shock layer attenuation of recession rate were made for selected combinations of velocity, altitude, nose radius, and particle size. The results were compared to predictions made based on a model incorporating AVCO breakup time and acceleration correlations. The results are summarized in the following table.

TABLE 4-1. SUMMARY OF NORMALIZED RECESSION RATE PREDICTIONS

Alt. (Kft)	Vel. (Kfps)	R_N (in.)	D_m (μ)	$\ddot{S}$	
				AERO	AVCO
12	13.2	.5	20 - 40	0.77 - 0.92	0.61 - 0.81
		1.0		0.43 - 0.77	0.16 - 0.54
		1.5		0.20 - 0.59	0.02 - 0.26
		2.0		0.08 - 0.43	0.00 - 0.09
6	11.4	1.0	100 - 200	0.94 - 0.97	0.82 - 0.92
		1.5		0.87 - 0.95	0.75 - 0.87
		2.0		0.79 - 0.94	0.54 - 0.80

The above table shows that for the relatively high altitude small droplet size case, shock layers begin to be effective relative to reducing recession rates for 1.0 inch nose radius vehicles and are extremely effective for 2.0 inch nose radius vehicles. For the lower altitude case the effects shown are significantly smaller; this is directly attributable to the fact that larger mean droplet diameters were employed for the low altitude cases.

The present model predicts smaller shock layer effects than does the model based on the AVCO data correlations. This is attributable to (a) present droplet acceleration effects are smaller than those reported by AVCO, (b) present values of breakup time are layer than those reported by AVCO. These differences reinforce each other relative to their impact on recession rate predictions. The differences in acceleration are small (less than 15 percent); however, the effect of these differences on recession rate predictions is significant (20 to 40 percent) since recession rate varies as the kinetic energy of the impacting particle. The differences between present and AVCO values of breakup time result from differences in interpretation of data. As previously described a more conservative approach was adopted in the present investigation.

The present results also show that deformation is significant up to much larger droplet diameters than breakup and acceleration; from this it can be concluded that droplet deformation effects on material response warrants investigation.

SECTION 5

REFERENCES

1. Hoglund, R. F., "Recent Advances in Gas-Particle Nozzle Flows," ARS J. 32, 662-671, 1962.

2. Gilbert, M., Allport, J., and Dunlap, R., "Dynamics of Two-Phase Flow in Rocket Nozzles," ARS J. 32, 1929-1930, 1962.

3. Carlson, D. J., Hoglund, R. F., "Particle Drag and Heat Transfer in Rocket Nozzles," AIAA J. 2, No. 11, 1980-1984, 1963.

4. Penner, S. S., Williams, F. A., Progress in Astronautics and Aeronautics, Vol. 6, Detonation and Two-Phase Flow, Academic Press, New York, 1962.

5. Wolfhard, H. G., Glassman, I., Green Jr., L., Progress in Astronautics and Aeronautics, Vol. 15, Heterogeneous Combustion, Academic Press, 1964.

6. Engel, O. G., "Fragmentation of Waterdrops in the Zone Behind an Air Shock," Journal of Research of the NBS, Vol. 60, Nov. 3, March 1958.

7. Nicholson, J., "Drop Breakup By Avistream Impact," Rain Erosion and Associated Phenomena, Royal Aircraft Establishment, Farnborough, England, Rep't. N68-19401-427, p. 342 — 369, 1967.

8. Ranger, A. and Nicholls, J., "Aerodynamic Shattering of Liquid Droplets," AIAA J., Vol. 7, No. 2, p. 285 — 290, February 1969.

9. Reinecke, W. G. and Wladman, G. D., "A Study of Drop Breakup Behind Strong Shocks with Application to Flight," Prepared by AVCO Systems Division, Wilmington, Mass. for USAF Space and Missile Systems Organization, SAMSO-TR-70-142, May 1970.

10. Aeschliman, D., "An Experimental Study of the Response of Water Droplets to Flows Behind Plane Shock Waves," Sandia Laboratories, SC-RR-71-0540, October 1971.

11. Waldman, G. D. and Reinecke, W. G., "Particle Trajectories, Heating, and Breakup in Hypersonic Shock Layers," AIAA J., Vol. 9, No. 6, p. 1040 — 1048, June 1971.

12. Reinecke, W. G. and Waldman, G. D., Shock Layer Shattering of Cloud Drops in Reentry Flight, AIAA Paper 75-152, presented at AIAA 13th Aerospace Sciences Meeting, Pasadena, California, January 20 — 22, 1975.

13. Jaffe, N. A., "Particle Decleration and Heating in a Hypersonic Shock Layer," Aerotherm TN-73-18, February 1973.

14. Jaffe, N. A., "Droplet Dynamics in a Hypersonic Shock Layer," AIAA J., Vol. 11, No. 11, p. 1562 — 1564, November 1973.

15. Finson, M. L., Lewis, P. F., Wu, P. K. S., Teare, J. D., Pirri, A. N., and Nebolsine, P. E., "Advanced Reentry Aeromechanics Interim Scientific Report," Physical Sciences Incorporated TR-10, August 1974.

16. Swain, C. E., Weber, W. T., and Timer, H. G., "Particle Shock Layer Interaction in Hypersonic Reentry," AIAA Paper 75-110, January 1975.

17. Swain, C. E., "The Effect of Particle/Shock Layer Interaction on Reenetry Vehicle Performance," AIAA Paper 75-734 presented at AIAA 10th Thermosphysics Conference, Denver, Col., May 27 — 29, 1975.

18. Dannenberg, R. E., and Humphrey, D. E., "Microsecond Response System for Measuring Shock Arrival by Changes in Stream Electrical Impedance in A Shock Tube," Rev. of Sci. Inst., Vol. 39, No. 11, p. 1692 — 1696, Nov. 1968.

19. Dannenberg, R. E., and Silver, A. F., "Arc Driver Operation for Either Efficient Energy Transfer or High Current Generation," NASA TM-X-62, 162, May 1972.

20. Dannenberg, R. E., "A Conical Arc Driver for High-Energy Test Facilities," AIAA J., Vol. 10, No. 12, pp 1692 — 1694, December 1972.

21. Abbott, C. E. and Cannon, T. W., "A Droplet Generator with Electronic Control of Size, Production Rate, and Charge," Rev. of Sci. Instr., Vol. 43, No. 9.

22. Sweet, R. G., "High-Frequency Oscillography with Electrostatically Deflected Ink Jets," Technical Report No. 1722-1, SEL-64004, Stanford Electronics Laboratories, Stanford University, Stanford, California, March 1964.

23. Hanson, A. R., Domich, E. G., and Adams, H. S., "Acoustical Liquid Drop Holder," Rev. Sci. Instr., Vol. 35, No. 8, August 1964.

24. Air Force, Handbook of Physics, Revised Edition, Macmillan, 1960.

25. Schmitt, G. R., Reinecke, W. G., Waldman, G. D., "Influence of Velocity, Impingement Angle, Heating, and Aerodynamic Shock Layers On Materials Erosion at Velocities of 5500 ft/sec," presented at ASTM committee G-2 Symposium on Erosion, Wear, and Interfaces with Corrosion, June 26 — 27, 1973.

APPENDIX A

A summary of test conditions and test results is given in Table A-1. This
table gives pressure upstream of the shock, shock velocity, droplet diameter, frame
number, time after passage of the shock for each frame, droplet displacement, dimen-
sionless time, deformation shape index, and dimensionless displacement.

TABLE A. SUMMARY OF TEST DATA.

Run	P (atm)	V (kfps)	d_0 (μ)	Frame	t (μsec)	x (mm)×10³	T	S	X
26	0.133	14.9	109	5	0.02	0	0.032	0	0
26	0.133	14.9	109	6	0.52	21.8	0.851	2.75	0.2
26	0.133	14.9	109	7	1.02	185.3	1.670	4.25	1.7
26	0.133	14.9	109	8	1.52	436	2.488	5.0	4
26	0.133	14.9	109	9	2.02	763	3.306	6.0	7
26	0.133	14.9	139	5	0.02	0	0.0256	0	0
26	0.133	14.9	139	6	0.52	0	0.667	2.5	0
26	0.133	14.9	139	7	1.02	55.6	1.309	4.00	0.4
26	0.133	14.9	139	8	1.52	166.8	1.95	4.75	1.2
30	0.122	15.2	140	4	1.15		1.44	3.75	
30	0.122	15.2	140	5	1.65		2.06	4.5	
30	0.122	15.2	140	6	2.15		2.69	5.5	
30	0.122	15.2	140	7	3.65		3.50	7.0	
34	0.130	15.6	180	2	0.04	0	0.041	1	0
34	0.130	15.6	180	3	0.54	0	0.557	2	0
34	0.130	15.6	180	4	1.04	45	1.10	3	0.25
34	0.130	15.6	180	5	1.54	180	1.59	4	1.00
34	0.130	15.6	180	6	2.04	360	2.10	?	2.00
35	0.139	15.5	95	2	0	0	0	0	0
35	0.139	15.5	95	3	0.497	0	0.996	2.5	0
35	0.139	15.5	95	4	0.997	95	1.99	4.0	1
35	0.139	15.5	95	5	1.497	380	3	6	4
48	0.134	11.1	53	1	1.20		1.5	3.5	
48	0.134	11.1	53	2	1.4		1.75	4.0	
48	0.134	11.1	53	3	1.6		2.00	4.5	
48	0.134	11.1	53	4	1.8		2.25	5.0	
48	0.134	11.1	53	5	2.0		2.51	5.5	
54	0.500	8.2	98	3	0.28	0	0.213		0
54	0.500	8.2	98	4	0.48	0	0.563	1	0
54	0.500	8.2	98	5	0.68	0	0.919	2	0
54	0.500	8.2	98	6	0.88	0	1.28	3	0
54	0.500	8.2	98	7	1.08	0	1.62	3.5	0
54	0.500	8.2	98	8	1.28	0	1.98	4.0	0
54	0.500	8.2	98	9	1.48	98	2.34	4.0	1
54	0.500	8.2	98	10	1.68	147	2.69	4.5	1.5
54	0.500	8.2	98	11	1.88	313.6	3.04	5.0	3.2
54	0.500	8.2	98	12	2.08	431.2	3.40	6.0	4.4
55	0.500	8.2	106	1	0.27		0	1	0
55	0.500	8.2	106	2	0.47		0.347	1.5	0
55	0.500	8.2	106	3	0.67		0.695	2.5	0
55	0.500	8.2	106	4	0.87		1.04	3.0	0
55	0.500	8.2	106	5	1.07		1.39	3.5	0
55	0.500	8.2	106	6	1.27		1.74	4.0	1
55	0.500	8.2	106	7	1.47		2.08	4.0	1.5
55	0.500	8.2	106	8	1.67		2.43	4.5	2.5
55	0.500	8.2	106	9	1.87		2.78	5.0	3.4
55	0.500	8.2	106	10	2.07		3.15	6.0	4.0

Run	P (atm)	V (kfps)	d_o (μ)	Frame	t (μsec)	x (mm)$\times10^3$	T	S	X
60	0.500	8.4	135	1	0.797	0	0.976	3	0
60	0.500	8.4	135	2	0.997	0	1.22	3.5	0
60	0.500	8.4	135	3	1.197	27	1.468	3.75	0.2
60	0.500	8.4	135	4	1.397	81	1.712	4.0	0.6
60	0.500	8.4	135	5	1.597	162	1.96	4.5	1.2
60	0.500	8.4	138	6	1.797	297	2.2	4.75	2.2
60	0.500	8.4	135	7	1.997	405	2.44	5.0	3.0
60	0.500	8.4	135	8	2.197	594	2.692	5.5	4.4
60	0.500	8.4	135	9	2.397		2.936	6.0	
63	0.500	9	100	1	1.51		2.7	5	
63	0.500	9	100	2	1.71		3.05	5.5	
63	0.500	9	100	3	1.91		3.42	6	
64	0.500	8.5	88	7	0.035		0.065	1	
64	0.500	8.5	88	8	0.235		0.44	1.5	
64	0.500	8.5	88	9	0.435		0.812	x	
64	0.500	8.5	88	10	0.635		1.19	3.0	
66	0.13	11.9	88	1	0.60		0.927		
66	0.13	11.9	88	2	0.80		1.24		
66	0.13	11.9	88	3	1.00		1.55		
66	0.13	11.9	88	4	1.20		1.85	3	
66	0.13	11.9	88	5	1.40		2.16	4	
66	0.13	11.9	88	6	1.60		2.47	4.5	
66	0.13	11.9	88	7	1.80		2.78	5	
66	0.13	11.9	88	8	2.00		3.10	6	
67	0.132	14.8	90	3	0.06		0.03	0	
67	0.132	14.8	90	4	0.408		0.80	2.5	
67	0.132	14.8	90	5	0.608		1.19	3	
67	0.132	14.8	90	6	0.808		1.58	4	
67	0.132	14.8	90	7	1.00		1.96	4.5	
67	0.132	14.8	90	8	1.21		2.37	6	
67	0.132	14.8	90	9	1.41		2.76	6.5	
70	0.132	11.7	110	3	0.07	0	0.10	1	0
70	0.132	11.7	110	4	0.27	0	0.38	1.5	0
70	0.132	11.7	110	5	0.47	0	0.67	2.0	0
70	0.132	11.7	110	6	0.67	16.5	0.96	3.0	0.15
70	0.132	11.7	110	7	0.87	33.0	1.24	3.5	0.30
70	0.132	11.7	110	8	1.07	88.0	1.53	4.0	0.80
70	0.132	11.7	110	9	1.27	143.0	1.81	4.5	1.3
70	0.132	11.7	110	10	1.47	220.0	2.1	5.0	2.0

DISTRIBUTION LIST

DEPARTMENT OF DEFENSE

Director
Defense Advanced Research Projects Agency
    ATTN: Strategic Tech. Office

Defense Documentation Center
12 cy ATTN: TC

Director
Defense Intelligence Agency
    ATTN: DT-2, Wpns. & Sys. Div.

Director
Defense Nuclear Agency
    ATTN: DDST
    ATTN: STSI, Archives
3 cy ATTN: SPAS
3 cy ATTN: STTL, Tech. Lib.

Dir. of Defense Rsch. & Engineering
    ATTN: AD/OS

Commander
Field Command
Defense Nuclear Agency
    ATTN: FCPR

Chief
Livermore Division, Field Command, DNA
Lawrence Livermore Laboratory
    ATTN: FCPRL

DEPARTMENT OF THE ARMY

Program Manager
BMD Program Office
    ATTN: DACS-BMT, Clifford E. McLain

Commander
BMD System Command
    ATTN: BDMSC-TEN, Noah J. Hurst

Commander
Harry Diamond Laboratories
    ATTN: DRXDO-NP

Director
U.S. Army Ballistic Research Labs.
    ATTN: Robert E. Eichelberger

Commander
U.S. Army Mat. & Mechanics Rsch. Ctr.
    ATTN: DRXMR-HH, John F. Dignam

DEPARTMENT OF THE NAVY

Chief of Naval Operations
Navy Department
    ATTN: OP-985D

Commander
Naval Sea Systems Command
    ATTN: 0333A, Marlin A. Kinna

DEPARTMENT OF THE NAVY (Continued)

Director
Strategic Systems Project Office
    ATTN: NSP-272, CDR Leslie Stoessl

DEPARTMENT OF THE AIR FORCE

AF Materials Laboratory, AFSC
    ATTN: MAS
    ATTN: MBC, Donald L. Schmidt
    ATTN: T. Nicholas

AF Rocket Propulsion Laboratory, AFSC
    ATTN: RTSN, G. A. Beale

AF Weapons Laboratory, AFSC
    ATTN: SUL

Commander
Foreign Technology Division, AFSC
    ATTN: TDFBD, J. D. Pumphrey
    ATTN: TDPTN

SAMSO/DY
    ATTN: DYS

SAMSO/MN
    ATTN: MNNR

Commander in Chief
Strategic Air Command
    ATTN: XPFS
    ATTN: DOXT

DEPARTMENT OF DEFENSE CONTRACTORS

Acurex Corporation/Aerotherm Division
    ATTN: N. A. Jaffe

Aerospace Corporation
    ATTN: Robert Herold

Avco Research & Systems Group
    ATTN: John Gilmore, E-502
    ATTN: William Reineke

The Boeing Company
    ATTN: Brian Lempriere

Effects Technology, Inc.
    ATTN: Robert Wengler

General Electric Company
Space Division
    ATTN: Phillip Cline, Rm. 3700
    ATTN: Walter Daskin

General Electric Company
TEMPO-Center for Advanced Studies
    ATTN: DASIAC

Institute for Defense Analyses
    ATTN: Joel Bengston

DEPARTMENT OF DEFENSE CONTRACTORS (Continued)

Kaman Sciences Corporation
   ATTN: Jerry L. Harper
   ATTN: John R. Hoffman

Martin Marietta Aerospace
Orlando Division
   ATTN: Laird Kinnaird

McDonnell Douglas Corporation
   ATTN: J. F. Garibotti

Physics International Company
   ATTN: Doc. Con. for James Shea

Prototype Development Associates, Inc.
   ATTN: John Slaughter

R & D Associates
   ATTN: F. A. Field

DEPARTMENT OF DEFENSE CONTRACTORS (Continued)

Science Applications, Inc.
   ATTN: G. Ray

Science Applications, Inc.
   ATTN: Lyle Dunbar

Stanford Research Institute
   ATTN: George R. Abrahamson

Systems, Science & Software, Inc.
   ATTN: Russell E. Duff

Terra Tek, Inc.
   ATTN: Sidney Green

University of Dayton Research Institute
   ATTN: Hal Swift